The Thesis Committee for Tao Yu
Certifies that this is the approved version of the following thesis:

Development of an Integrated Expansion Evaporator and Condenser Unit for an Advanced Thermo-Adsorptive Battery System

APPROVED BY
SUPERVISING COMMITTEE:

Supervisor:

Li Shi

Carlos H. Hidrovo

Development of an Integrated Expansion Evaporator and Condenser Unit for an Advanced Thermo-Adsorptive Battery System

by

Tao Yu, B.E.; B.S.M.E.

Thesis

Presented to the Faculty of the Graduate School of

The University of Texas at Austin

in Partial Fulfillment

of the Requirements

for the Degree of

Master of Science in Engineering

The University of Texas at Austin

August 2014

Dedication

To all my families and friends who have been amazingly supportive throughout my master journey.

Acknowledgements

First of all, I want to thank Dr. Hidrovo for all the guidance he offered throughout the project. The motivations from him always drove me to a higher level of understanding. I also want to thank Dr. Myeongsub Kim, Dr. Carlos Rios, Dr. Tae Jin Kim, Renee Hale and the rest of Multiscale Thermal Fluids Laboratory Group. The advice and hands-on help from them is indispensable to the success of my research and the lovely accompanying time with them has definitely become one of the most precious parts of my memories.

I would acknowledge that some part of the research work recorded in this thesis come from the undergraduate research assistants who worked in this project. Collier Miers and Geoff Wehmeyer started this project before me and they have a tremendous contribution to the early design phase of the coolant loop and the refrigerant delivery system. They also did a great job recognizing the early schematic for the monolithic system setup. Spencer Dorr provided extremely important hands-on help to the vacuum test setup and testing. Spencer and Collin Capello are the major contributors who built up the monolithic system test setup from scratch. Gerardo Velez played an important role when I needed help during the prototype fabrication process. I cannot express in words how much I do appreciate their support in this project.

Finally, I want to express my gratitude towards Dr. Li Shi for graciously serving as my reader and helping me out of the difficult situation during our lab transition.

Abstract

Development of an Integrated Expansion Evaporator and Condenser Unit for an Advanced Thermo-Adsorptive Battery System

Tao Yu, M.S.E

The University of Texas at Austin, 2014

Supervisor: Li Shi

The advanced thermo-adsorptive battery climate control system (ATB) is a highly innovative cooling and heating technology being developed by a cross-disciplinary academic and industrial team. The primary goal of this technology is to be employed in electric vehicles (EVs). In comparison with the conventional vapor-compression cooling system and the inefficient resistive heating method employed by the EVs' industry, the ATB system is expected to offer EVs an additional 30% driving range by providing high cooling (2.5kWh) and heating (3.5kWh) storage in a lighter (<35kg) and more compact (<30L) system.

The integrated expansion evaporator/condenser unit (IEECU) is one of the most crucial components comprising the ATB system. It combines the functions of an evaporator and a condenser and is designed to enhance the heat exchange between coolant and refrigerant. This thesis summarizes the work starting from the design, fabrication to characterizing process, with a particular focus on evaporation characterization.

Development of ATB system and test setup including other components is covered in the rest of thesis.

Table of Contents

List of Tables

List of Figures

List of Equations

Chapter 1: Introduction

1.1 MOTIVATION

Global warming is one of the most concerning climate-change challenges faced by human beings. High emission of CO_2 has been the dominant factor worsening the situation. As the leading CO_2 emission sector, transportation has attracted lots of attentions from legislators, regulators and entrepreneurs, who are looking for real changes. One of the huge efforts has been spent on replacing combustion-engine vehicles with electric vehicles (EVs), which can drop CO_2 emissions during driving to zero. The development history of electric vehicle is long and because of many factors, the pace has been slow until very recently. As of 2013, the EVs' market share of total new car sales in the United States is only 0.62% [1], nearly negligible.

However, factors like soaring price of gasoline, tax incentives, people's fascination with the newer technology, and rising environmental awareness have generated a recent stimulus for a growing demand of EVs worldwide. As of December 2012, there were over 180,000 highway-capable plug-in electric passenger vehicles and utility vans worldwide [2], while in the U.S. over 11,000 EVs were sold as of August of 2013 [2]. Despite the gradual increase in EVs however, there continues to be significant battery-related challenges. Among them, the low energy storage density of lithium-ion battery widely used in EVs today seriously limits their driving ranges on a single charge, let alone offers comfortable heating or cooling to passengers. Conventional climate-control systems used in EVs can reduce the driving range by as much as 30%. 100 miles is the average driving range of EVs today on a single charge [3], and Tesla claims its Model S can drive up to 200 miles, but that is as far as EVs can go on this planet without charging. Comparing to combustion-engine vehicles, the driving range anxiety

undoubtedly makes people think twice before purchasing an EV. In general the 30-70% shorter driving range due to low energy density of lithium-ion battery has become one of the bottlenecks for EVs development. Furthermore, since current technologies for managing EVs' climate control system (heating and cooling needs of the cabin) significantly drains the battery, driving range is further reduced by more than 30% at the peak power drainage. By using an Advanced Thermo-Adsorptive Battery Climate Control System (ATB) however, this reduction in driving range, due to climate control, can be completely eliminated.

1.2 BASICS OF CAR HVAC

Conventional vehicles use internal combustion engine (ICE) waste heat and shaft work to provide heating and cooling air to the passenger compartment [4], respectively.

Engine coolant absorbs heat from ICE and rejects the same amount of heat through an air-to-liquid heat exchanger in front of cabin. In the meantime, the air blown through the heat exchanger delivers this heat to the cabin and brings thermal comfort to passengers.

Cooling mode generally employs a vapor-compression cycle and needs a separate air-conditioning fluid loop. Mechanical power from the engine is diverted to run a compressor, which circulates ~ 1kg of refrigerant through a basic refrigeration cycle. The condenser and fan are often located just in front of the radiator at the vehicle's nose, while the evaporator and blower are located at the rear of the engine compartment near the passenger cabin and in some cases utilize the same ducting as the heating system [5].

Typical ICE vehicle cooling units have overall masses ranging from 12-22 kg and maximum cooling capacities from 3-8kW. The coefficient of performance or COP is a parameter widely used to describe heat pump performance. It is a ratio of heating or

cooling provided to electrical power consumed. COP for the refrigeration cycle ranges from an average of ~4 at 0ºC to ~1 at 50ºC [5]. Because ICE vehicles integrate the engine cooling and cabin heating systems, the heating COP is less meaningful. However, typical heater cores add 2-6kg to the engine cooling system mass and handle heat fluxes in the kW range [5, 6]. Together, the heating and AC subsystems form the largest ancillary load on the ICE vehicle drivetrain by an order of magnitude [7].

1.3 Background on Thermal battery

Thermal battery is a general term for energy system that utilizes thermophysical or thermochemical materials to store useful energy, usually in a more sustainable way.

Electric vehicles, which today can draw as much as 35 to 40% of their electrical battery capacity for cabin heating and cooling, could dramatically increase their driving range by using a separate thermal battery, charged from the grid or waste-heat sources, for cabin conditioning [8]. Even conventional combustion-engine vehicles could use thermal storage to avoid cold-engine starts, which can temporarily reduce fuel efficiency by 10% or more, depending on the ambient temperature [9]. When connected to the electricity grid, thermal storage would offer the added benefit of load shifting for applications such as air conditioning or refrigeration [10], or it could be used directly to store electricity from the grid [11].

1.4 Technology description of the ATB Climate Control System

The ATB climate control system falls into the thermophysical class. In the ATB system, the refrigerant, water, is pumped into a low-pressure vessel during operation. The vacuum pressure can be as low as 760 Pa and the boiling point of water drops to 3 °C in this vacuum. As soon as being injected into the vessel, ambient-temperature water

evaporates and absorbs heat as in a phase change process. This evaporative cooling can be utilized to lower the temperature of the air that is vented into the passenger cabin.

The adsorption beds, which are filled with a special high-capacity material, pull the water vapor out of the integrated expansion evaporator/condenser unit (IEECU) to keep the vacuum pressure constantly low so that more water can be evaporated. The adsorption material has a property of releasing heat while adsorbing water molecules. The heat can either be utilized to warm the cabin or be rejected into the atmosphere by a radiator if not needed.

After approximately 4-hour operation, the adsorption material becomes saturated with water, so the thermal battery system has to be recharged. The regeneration cycle is performed at the same time as the electrochemical battery being charged. It is simply an electrically heating process, which forces water molecules to escape from the adsorption beds. Once water vapor is desorbed from the beds, it gets condensed on the IEECU and turns into liquid phase. Finally, liquid water is collected in the reservoir for subsequent cycles.

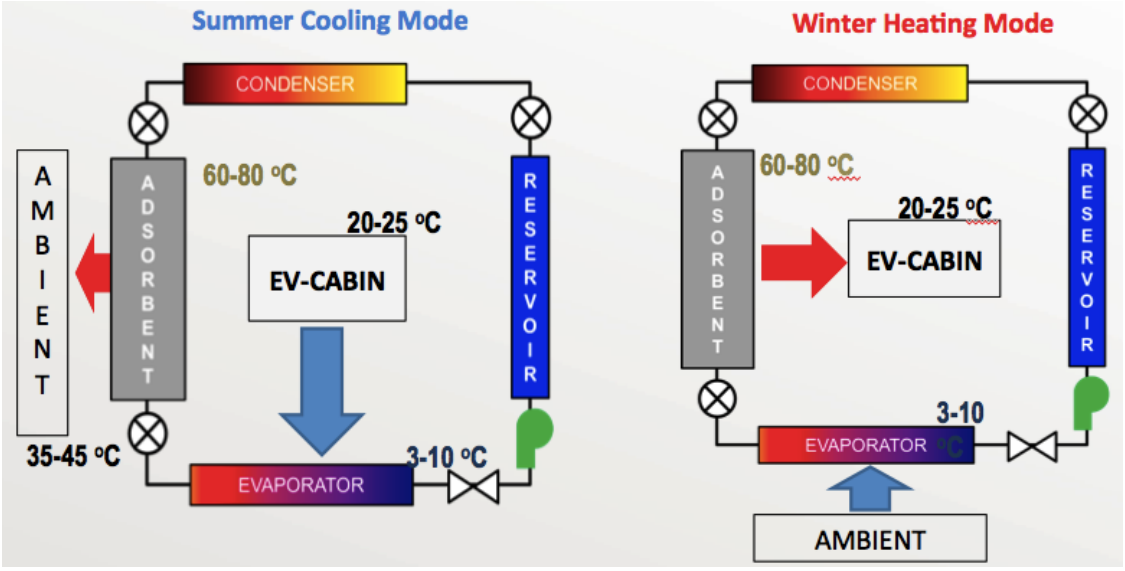

Figure 1.1: ATB system working mechanism

Chapter 2: IEECU Design

Unlike a regular heat exchanger, where sensible heat is exchanged between two media at different temperatures, the IEECU is a heat exchanger that makes use of the latent heat of the refrigerant vaporization process to absorb heat from the coolant. It is comprised of a coolant loop and a refrigerant delivery system. As seen in Figure 2.1, the coolant enters the enclosed IEECU from the antifreeze tubes at a relatively higher temperature, while the refrigerant is spread over outer fin surfaces by the delivery system so that it can be evaporated under the vacuum. The coolant flow is a means of providing heat to evaporate the refrigerant. As the coolant flowing across the IEECU, the temperature of coolant keeps decreasing due to evaporative cooling on the outer surfaces. The coolant temperature is low enough to provide cooling effects to passengers when it exits the IEECU. During the whole heat exchange process, the coolant and refrigerant are not in contact with each other.

For the coolant loop, by studying the interior structures of an existing evaporator, a double-fin coolant passage with sophisticated dimple and mini-channel geometries was developed. The double-fin coolant fin structure shown in Figure 2.1 is constructed from two aluminum sheets stamped with indentation. Coolant enters the heat exchanger through a manifold and is diverted past the stamped horizontal cylinders and conical sections between the fin plates. Thanks to these barricades, the flow is maintained in a constantly developing fashion and contact area for heat exchange between coolant and refrigerant is increased by about 40%.

A heat transfer and fluid flow model was developed in Matlab to find out the optimum coolant flow rate, at which both the 2.5 kW heat dissipation rate and a reasonable temperature drop between the inlet and outlet can be achieved.

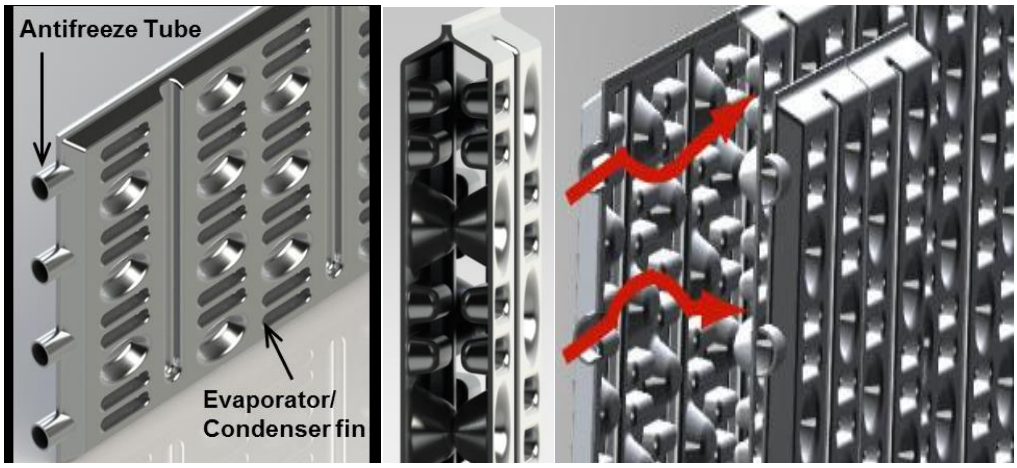

Figure 2.1: IEECU coolant loop design

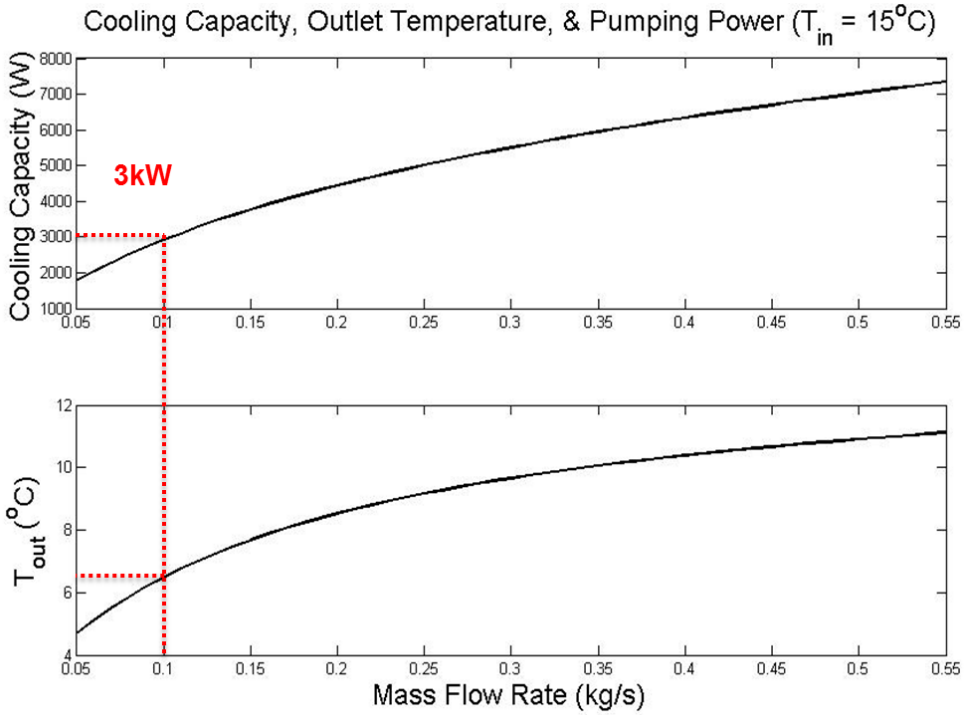

Figure 2.2: Thermal characteristics of the IEECU coolant loop design. At a glycol inlet temperature of 15 °C, a flow rate of glycol at 0.1 kg/s is required to achieve more than 2.5 kW and around 7 °C temperature drop from the inlet to the outlet.

In terms of the refrigerant delivery system, 1) droplet spray and 2) porous media (PM) design were investigated. Since they have different heat transfer and hydrodynamic mechanisms, separate analyses were performed and results were compared to decide the ultimate approach.

There are metric requirements from three perspectives that lead the design process. From heat transfer perspective, the design has to guarantee 2.5kW of heat transfer between coolant and refrigerant. The working conditions for the refrigerant are supposed to be 3°C and 760 Pa at the evaporation site. From pressure drop perspective, during the operation, the pressure inside the refrigerant reservoir is higher than that at the IEECU site due to previous desorption process. Whether this pressure difference is strong enough to drive the refrigerant to the evaporation site or extra pumping power is necessary was determined through hydrodynamic calculation. From spacing perspective, either design has to be restricted in an approximately 5cm x 8cm x 78cm space. Other factors such as ease and cost of manufacturing were also taken into consideration while creating and evaluating two designs.

2.1 SPRAY COOLING DESIGN

Spray cooling, especially at low pressures, has been shown to be one of the best cooling techniques for applications that require efficient high heat flux removal [11]. Marcos's experiments have shown that at 0.015bar, the maximum overall heat transfer coefficient of 113,000 W/m^2K and more than a 50% reduction in surface temperature can be achieved by utilizing spray cooling in a low-pressure environment [5]. Temperature of refrigerant droplets, which in our case are water droplets, has to be lower than that of the target surface, which needs to be cooled. By releasing heat to the droplets and the thin film on the target surface to provide enough energy for evaporation, IEECU removes a

bulk amount of heat from the coolant. For this project, the saturation temperature associated with the bed pressure (760Pa) is 3 °C.

The pressure nozzle is also called the plain-orifice atomizer. A huge pressure drop across the orifice is able to break up liquid phase water into small droplets. Higher pressure drops and smaller orifice diameters can deliver finer droplets.

The size of the nozzle is determined by evaporation efficiency. Once droplets land on the evaporator fin surface, they are expected to change into vapor phase immediately. This evaporation efficiency was defined as the percentage of the total heat that could be removed by the spray, including sensible and latent heat, at critical heat flux [12].

$$\eta = \frac{q''_m}{q''_{dryout}} X\ 100\ \% = \frac{q''_m}{\rho_{water}\overline{Q''}\ h_{fg}(1 + C_{p,f}\Delta T_{sub}/h_{fg})} X\ 100\%$$

The inlet temperature of water is maintained at 3°C, as will be explained in depth in the heat transfer analysis section. Consequently, there is no sensible heat removed by the spraying. The 2.5kW metric cooling rate can only be achieved when evaporation rate on the fin surface reaches 1g/s. Figure 2.3 [12] serves as an illustration showing a relationship between evaporation efficiency and spray Weber number We.

$$We = \frac{\rho_f \overline{Q''}^2 d_{32}}{\sigma}$$

In the equation above, there is another new parameter d_{32}, which stands for Sauter Mean Diameter (SMD). SMD is used to estimate the average size of water droplets in a spray pattern. A nearly 100% evaporation efficiency can be achieved for We < 10^{-5} and 10% for We > 0.1.

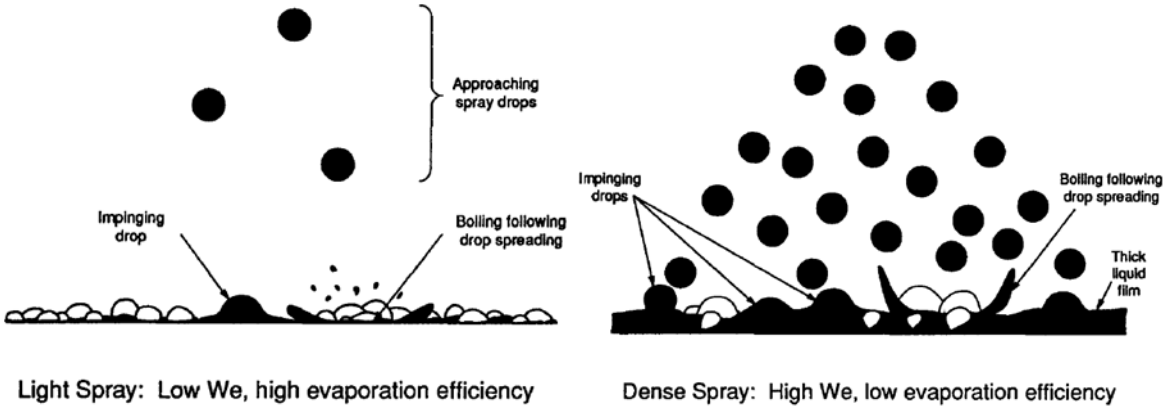

Figure 2.3: Schematic showing boiling under light (left) and dense (right) sprays

200 μm SMD is needed to guarantee 100% evaporation efficiency. Based on corresponding equations and SMD correlation figure in Estes and Mudawar[12], to create a spray pattern with SMD = 200 μm, a pressure drop across 700 μm-diameter nozzle needs to be equal to or higher than 76kPa. The water reservoir is at 20 kPa, so an extra pressure head of 56 kPa needs to be provided by a pump upstream.

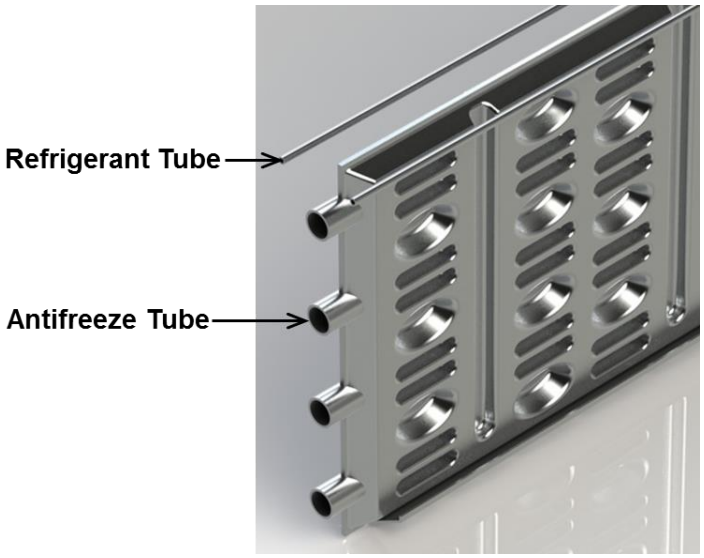

Figure 2.4: Spray Cooling Design

Dr. Yanosy has conducted extensive experimental work on water spray cooling under vacuum [13]. The pressure of his experiment went as low as 800 Pa, which is close to the ATB system operating pressure to 760 Pa. The empirical equations were used while creating the spray cooling design.

As seen from Figure 2.3, two 1.0 mm-diameter refrigerant tubes are mounted on each side of the vertical evaporator fin channel. The tips of the refrigerant tubes are at the same height with the top of the evaporator fin surface. The horizontal distance between the channel and each refrigerant tube is about 3.5 mm. 75 spray nozzles are spaced evenly along each 75-cm long tube. The nozzle alignment axle is tilted inward from the vertical plane by 25°, as seen in Figure 2.4.

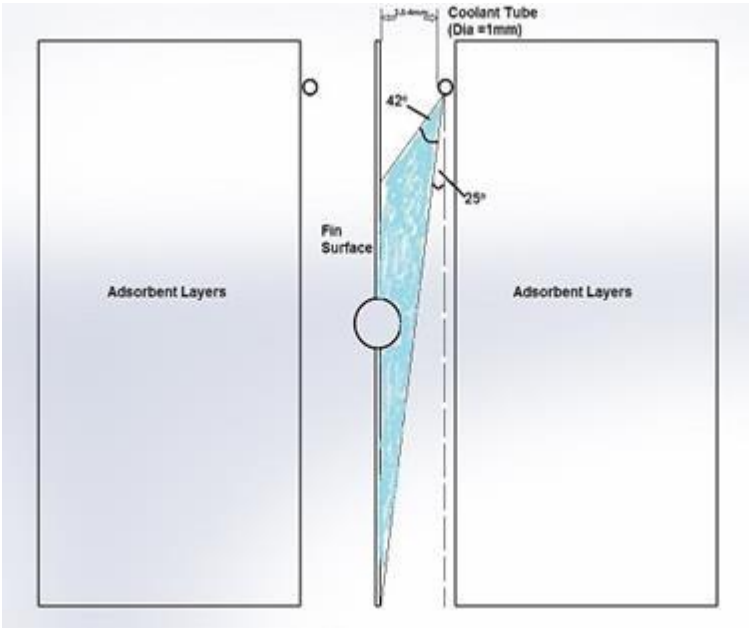

Figure 2.5: Refrigerant tube configuration

Sauter Mean Diameter (SMD) is widely used to characterize the average droplet size in the spray-cooling field.

$$SMD = 3165\Delta P_n^{-0.675} t_f^{*0.375} \sigma^{0.51} \qquad W_e < 1$$

$$SMD = 110\Delta P_n^{-0.275} t_f^{*0.375} \sigma^{0.16} \qquad W_e > 1$$

After research on common micro-size nozzles and the predetermined coolant tube diameter (1mm), the nozzle diameter was further decreased to be 250 μm, which is one fourth of tube diameter. The relationship between pressure drop and SMD can be plotted below based on correlations above.

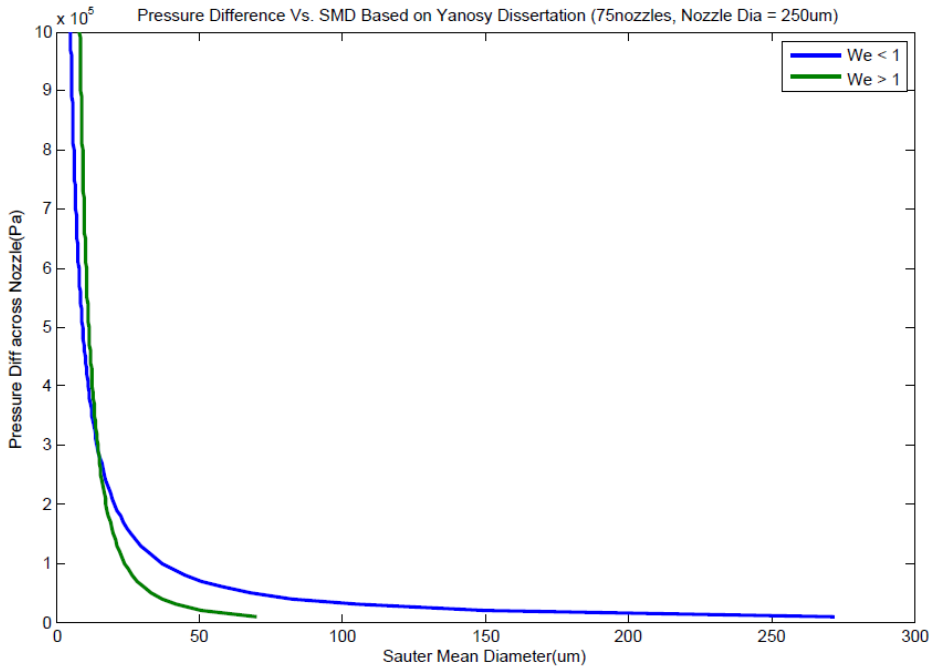

Figure 2.6: Pressure Difference vs. SMD

Overall, at least 0.05Mpa has to be provided in order to generate desired spray pattern and SMD. However, Mudawar's correlation generally requires a higher pressure difference across the nozzle, which is at least 0.5Mpa. 0.5Mpa was then chosen for experimental validation purpose.

Based on a heat transfer coefficient empirical equation provided in Yanosy's dissertation, a maximum heat transfer coefficient of 6500W/m^{2}K can be achieved. The evaporator fin surface area is 0.12-0.14 m^2. To achieve 2.5kWh cooling metric target, the average temperature difference should not be smaller than 3.2°C. The assumption is that the evaporator fin surface temperature is around 3°C and coolant enters at 15°C and exits at 5°C, it is very probable for the spray cooling design to meet the heat transfer criteria.

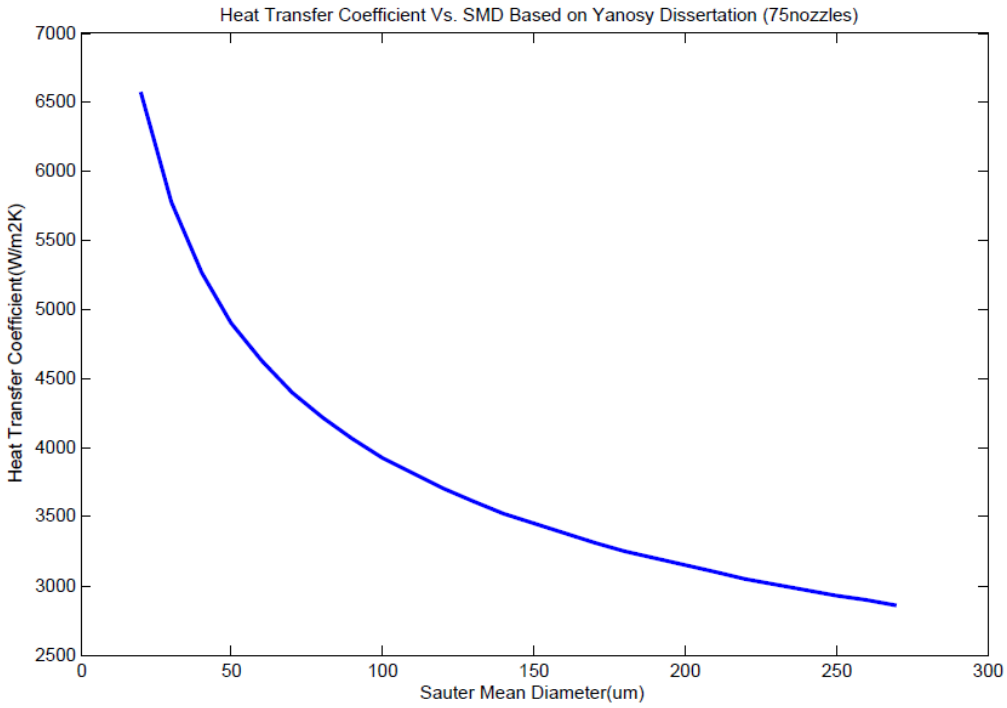

Figure 2.7: Heat transfer coefficient correlation

2.2 POROUS MEDIA DESIGN

The PM design shown in Figure 2.8 utilizes layers of sintered copper porous media on top of refrigerant distribution mini-channels. During operation, the refrigerant experiences a pressure drop and enhanced thin-film evaporation on top of porous media [14]. To achieve a saturation temperature at 3 °C, the refrigerant pressure needs to be reduced to 760 Pa when it arrives at the evaporation site. The pressure of the water in the

reservoir is assumed to be 20 kPa. To achieve the pressure drop from the reservoir and the evaporation site, two methods can be used.

Sudden pressure drops, usually achieved by using valves, have already been discussed in the last section. The other method, gradual pressure drops, can be achieved by layering porous media on top of refrigerant flow channels. A 5.7 mm layer of 10 micron diameter copper particles sintered at 550 °C for 180 minutes would provide a 20 kPa pressure drop with the 1g/s liquid water flowing onto the evaporation site.

During regeneration process, water vapor that has been desorbed condenses in films on the porous media, and drains into a trough underneath the evaporator. Sintered copper was studied because of the porous media's low permeabilities (10^{-13} to 10^{-12} m^2), high mechanical strength, and relatively large thermal conductivites (50-350 W/mK) as described in a recent experimental investigation [15].

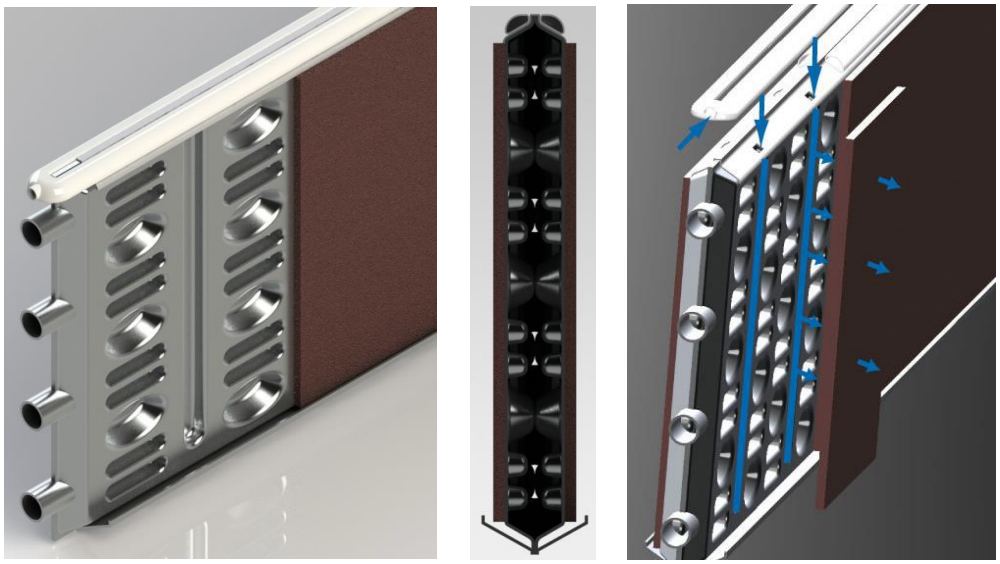

Figure 2.8 Porous media design

2.3 ANALYTICAL COMPARISON BETWEEN PM DESIGN AND SPRAY COOLING DESIGN

Table 2.1 displays the criteria used for selecting a heat exchanger. The required pumping powers during operation and the thermal resistance to evaporative heat transfer were on similar orders of magnitude for each design. The failure risks for each design would need to be mitigated and checked in any final assembly. The droplet formation in spray cooling acts as a sudden isenthalpic expansion, while the aspects of expansion through the porous material are less confined.

It did not result in a clear decision in favor of either design. Proof-of-concept experiments were created to determine which design would perform better during operation and to evaluate the ease of manufacturing and testing of a prototype.

Table 2.1: IEECU Spray Cooling and PM Design Comparison

Spray Cooling		Metric		Porous Media
0.5 – 5 W (1 g/s pumped to 500 kPa or 5 MPa)		Refrigerant pump work during operation		0 W (Reservoir placement for gravity feed)
1.5 * 10^{-4} (m^2K/W)		Thermal Resistance ($R_{th} = \frac{\Delta T}{q''}$) between fin and evaporation)		9.2 * 10^{-5} (m^2K/W) from conduction : Comparable with experimental data.
15 – 40 W		Pumping power during operation		10-35 W
Drilling 250 um nozzle difficult	✓	Ease of mass manufacturing	✓	Minichannels stamped with antifreeze pattern Porous media sintering for attachment
12 g/s	✓	Condensation Rate (T_{fin}= 30°C, T_{desorb} = 60 °C)		1.4 g/s [Increases with increasing permeability]
Pump controls flow during operation		Hydrodynamic Simplicity		Thermostatic expansion valve passively regulates the system
Two studies on SC at reduced pressures. UT group droplet experience.		Precedence and group experience		Many papers on porous material fabrication, MIT and UT group experience with PM.
Spray on adsorbent due to hole fouling. Film formation on glycol fin.		Failure Risks		Pressure drop not achieved. Two-phase flow in supply/porous media traps vapor. Contact Resistance
Spray concerns when vehicle is on banked curve		Versatility		Gravitational effects for vehicle on steep hill
Better regeneration and rapid expansion	✓	Cycle Performance		Gradual expansion and longer regeneration

Chapter 3: Proof-of-concept testing

Proof-of-concept experiments were performed to further validate previous evaluations on the PM design and spray cooling design. The ultimate goal was to pick a primary design and continue the prototype fabrication and characterization testing based on the primary design. The proof-of-concept testing started with tests at atmospheric pressure, and was modified and moved into a vacuum chamber.

3.1 PROOF-OF-CONCEPT EXPERIMENTS AT ATMOSPHERIC PRESSURE

At this preliminary test stage, the operating pressure was set to be atmospheric pressure. Correspondingly, the saturation temperature is increased from 3°C to 100°C. At the moment of testing, the evaporator fin prototype was not fabricated yet, so there was no coolant flow involved at this stage. As seen in Figure 3.1, four cartridge heaters were inserted into a base copper plate to provide a constant power supply so that refrigerant, in this case, water evaporated at a constant rate. The whole prototype was enclosed by G10 insulation layers (green). For PM set up, since sintering technique for porous media was not mature, 20 layers of 10 μm-size copper meshes were stacked together to provide the equivalent porosity (60%) and permeability ($0.7x10^{-13}m^2$). The copper plate with a water channel in the middle was used for dispersing water evenly and it act as the evaporator fin surface but without any dimple or groove structures. Thermocouple locations are labeled in the figure. For the spray cooling design, the same prototype was utilized. The copper meshes were taken off and water droplets got sprayed onto the channel copper layer directly. Actual test setups for both designs are shown in Figure 3.2.

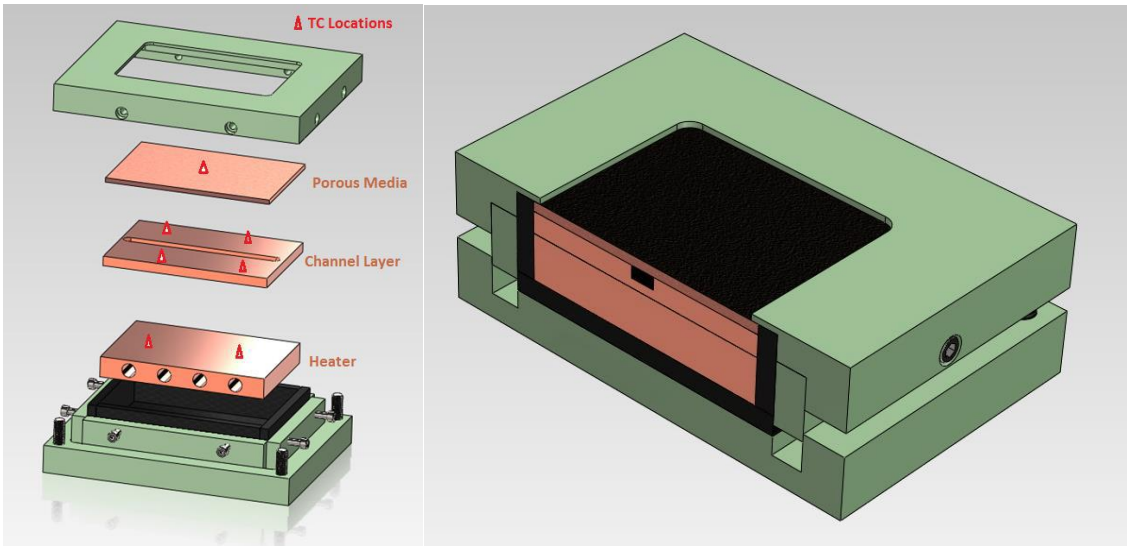

Figure 3.1: Model of prototype

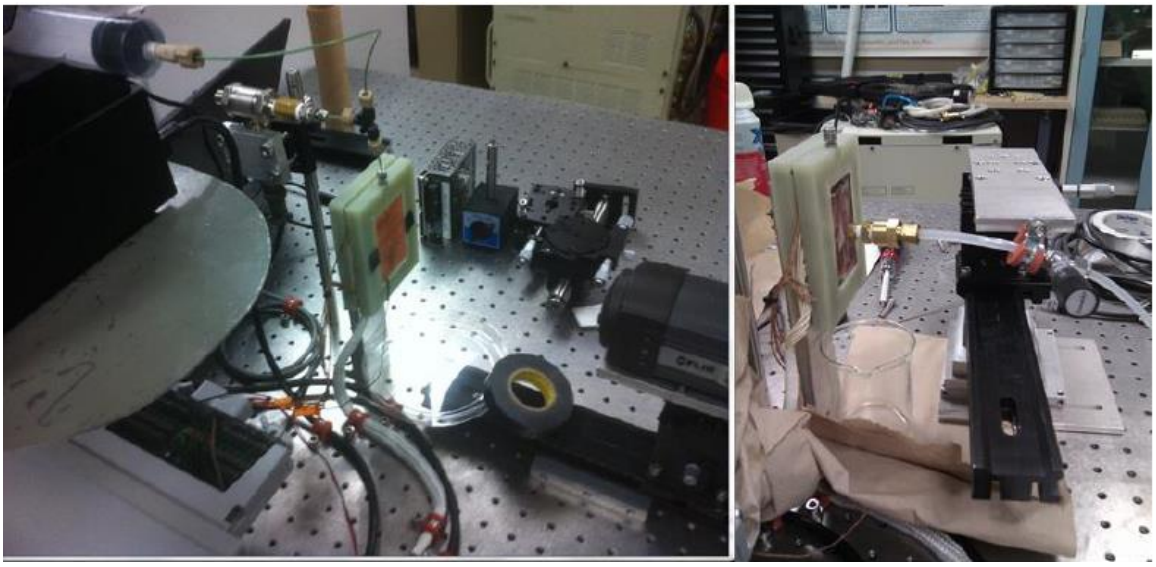

Figure 3.2: Test setup for PM design (left) and spray cooling design (right)

In the actual porous media design, there are 30 mini-channels in total, 15 on each side of the evaporator fin surface. In previous sections, it was mentioned that 1g/s evaporation rate has to be achieved to reach 2.5kW cooling metric target, which means

on average 1/30 (0.033) g/s liquid water flows down through each channel. The latent heat of water is 2260kJ/kg, so in order to vaporize the liquid water at a rate of 0.033g/s, at least 87W heat has to be provided by heaters. Figure 3.3 shows the temperature profiles measured at the top and bottom of the mini-channel plate, where evaporation mostly happened. After the heater was turned on, the temperature quickly increased up to 130°C at the top location and right after water was injected into the mini-channel, it stabilized at 100°C, which is the saturation temperature at atmospheric pressure. This suggests that the PM design can provide enough evaporation capacity at room temperature and atmospheric pressure.

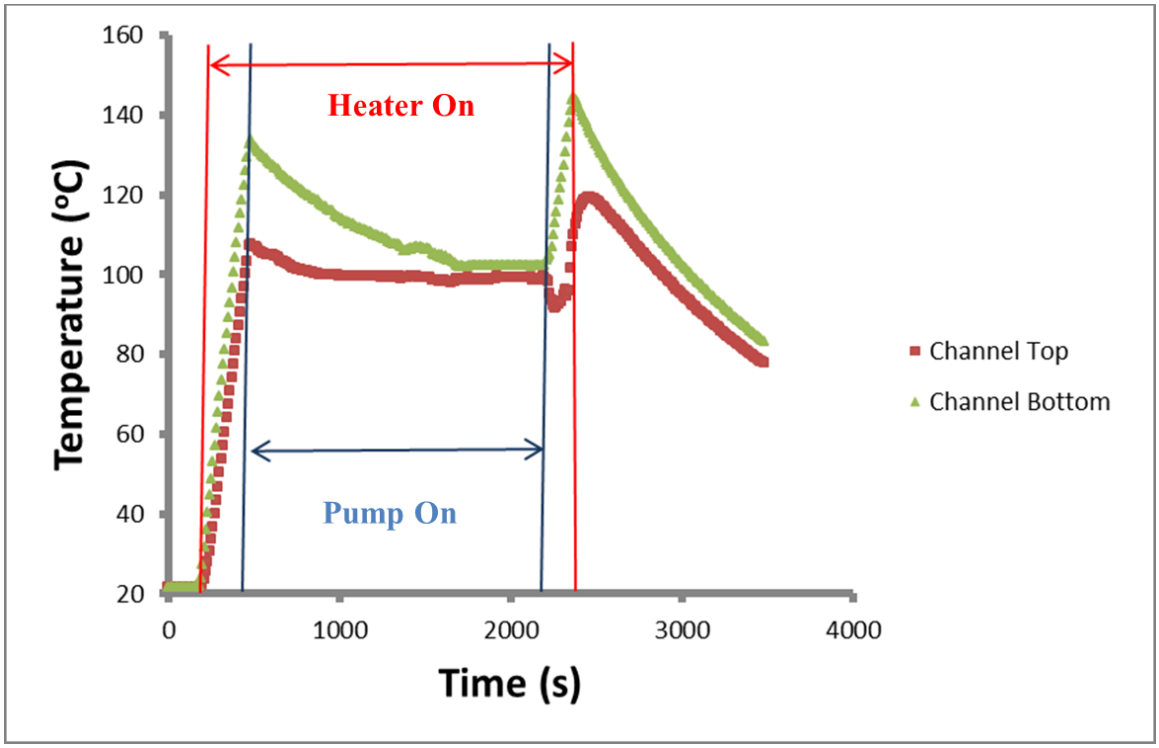

Figure 3.3: Preliminary ambient testing results on PM design. The temperatures increased because the heater was on. The temperature decreased because the syringe pump started to inject water into the mini-channel and evaporation cooled down the surface.

During preparation of the spray cooling test setup, it was realized that drilling a 200 μm-size nozzle on a 1mm-diameter tube was more difficult than expected. When directly connecting a 200μm-diameter tube to a pump, only water jet shot out of the tube outlet instead of a desired water spray pattern. It suggested that the pressure before the outlet was very low due to pressure loss upstream in this tiny tube. This hurt the chance of spray cooling design being selected as the primary design since ease of manufacturing and maneuverability should be under consideration. At this stage, a commercial mist nozzle with 200μm-diameter orifice was used to generate the desired spray pattern, as seen in Figure 3.2. During PM design tests, 0.033g/s water supply was maintained by a syringe pump, but the syringe pump could not provide enough pressure head for the mist nozzle to generate a spray, so a high pressure diaphragm pump replaced the syringe pump in the spray cooling tests. The downside of this diaphragm pump was that the minimum water flow rate achievable was 0.1g/s, so the input power for the heaters was ramped up to 261W, which is three times of that for the PM test. Temperature readings were collected at the bottom of the mini-channel plate, as seen in Figure 3.4.

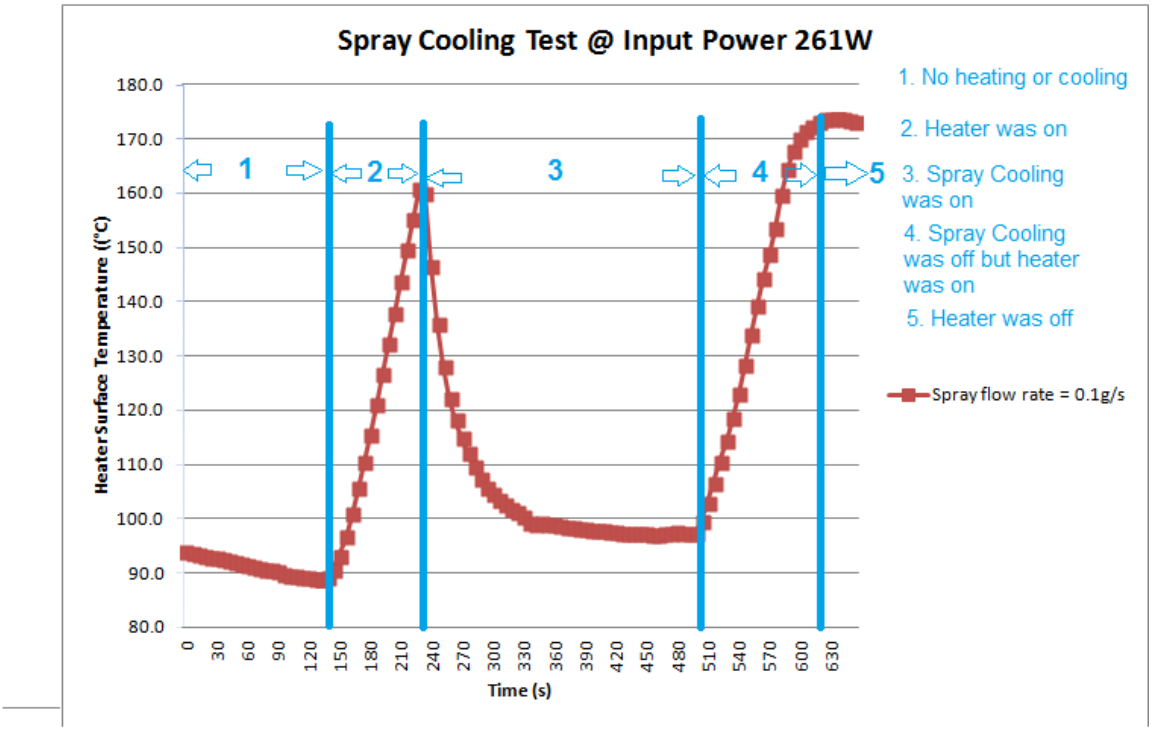

Figure 3.4: Preliminary ambient testing results on spray cooling design. Phase 1, heater was off and no water was injected; phase 2, heater was turned on and temperature started to climb since no water was injected yet; phase 3, water was sprayed onto the prototype surface and cooled down the temperature; phase 4, heater was still on but water supply was shut off; phase 5, heater was turned off.

The test started without heat or water input. After the heater was turned on, the temperature went up but immediately dropped down when the nozzle started to spray water onto the surface. Similar to the PM design test results, eventually the temperature stayed around 100°C, which is the saturation temperature of water at atmospheric pressure. This indicated that the heating and cooling power were equivalent to each other and the energy balance reached equilibrium.

The initial tests suggested that the evaporative cooling worked at atmospheric pressure for both designs. But the difficulty of achieving a fine droplet sprays with the

current spray cooling design made the PM design the primary choice for further prototype testing and fabrication. Tests under vacuum conditions for the PM design followed up to understand how the IEECU prototype reacts to a low pressure environment.

3.2 PROOF-OF-CONCEPT EXPERIMENTS IN VACUUM

The prototype test rig was modified for vacuum testing. The clearance between the copper plates and the G10 housing was further reduced to eliminate possible water leakage and two crosspieces were added on the top G10 compartment to prevent porous media bulging out of the housing, as seen in Figure 3.5.

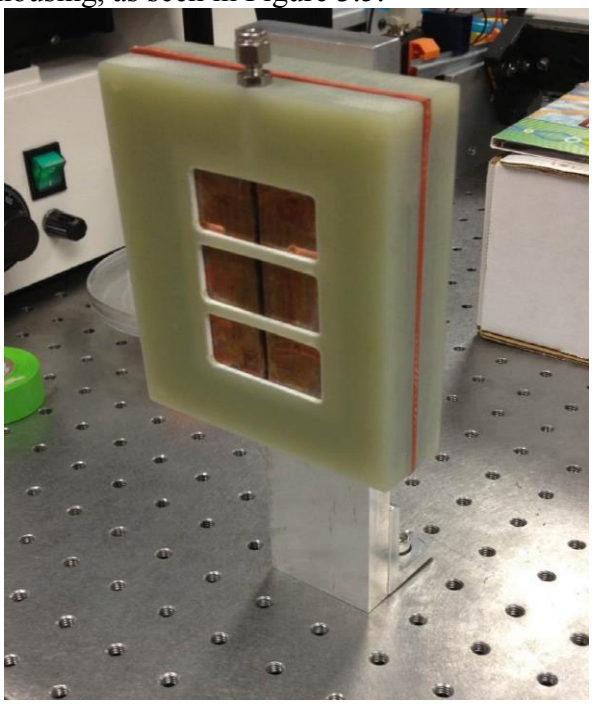

Figure 3.5: Modified PM design prototype test rig

The PM test rig with cartridge heaters and thermocouples were placed in a vacuum chamber, shown in Figure 3.6.

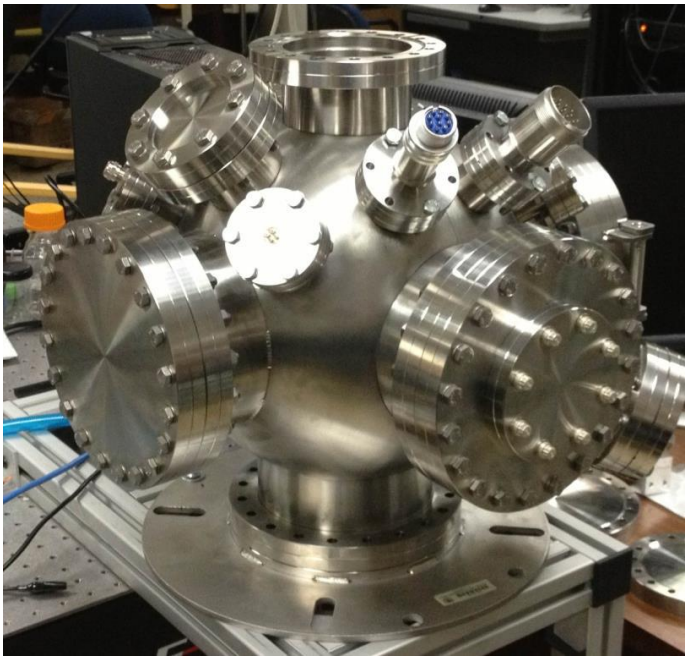

Figure 3.6: Vacuum chamber for testing

The whole setup consists of three sub-systems, including the water feeding system, a vacuum chamber and the air/vapor outlets, as seen in Figure 3.7 and Figure 3.8.

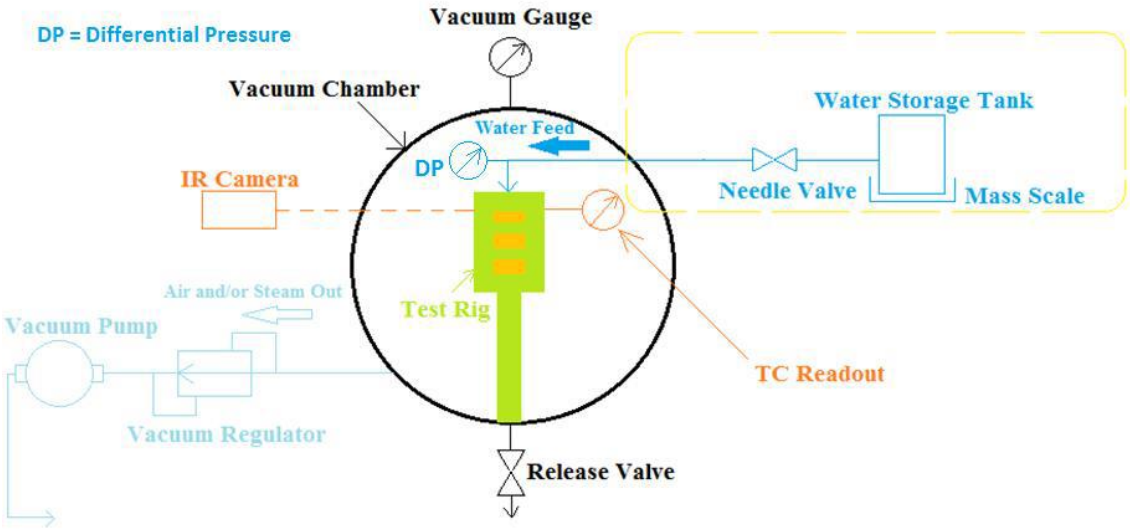

Figure 3.7: Vacuum test set-up diagram

For the water feeding system, a water reservoir was placed on an AMD mass scale, which transferred mass readings to a computer, and a Labview program was written to monitor the instantaneous mass flow rate leaving the reservoir. A Swagelok needle valve was used to set the desired flow rate (2g/min) from the water delivery line.

A pressure transducer (Omega PX409) was mounted on the chamber to monitor the absolute pressure inside. As seen in Figure 3.1, there were seven T-type thermocouples attached on different locations of the copper plates to monitor the temperatures: one right in front of the porous media, four underneath the porous media, and two between the mini-channel plate and the heater plate. All the temperature readings, input power for the heaters and pressure readings were transferred through a special signal feedthrough flange to the Agilent 34980T DAQ sitting outside the vacuum chamber, as shown in Figure 3.8.

There were no real adsorbents inside the vacuum chamber to adsorb water vapor generated during operation, so a ULVAC vacuum pump was interfaced to suck the water vapor out and maintain the desired vacuum pressure of 760 Pa. A vacuum regulator was employed to control the vacuum level along the vacuum line. Meanwhile, an infrared camera was positioned in front of the observation window of the vacuum chamber so that thermal images of the porous media surface could be obtained during testing.

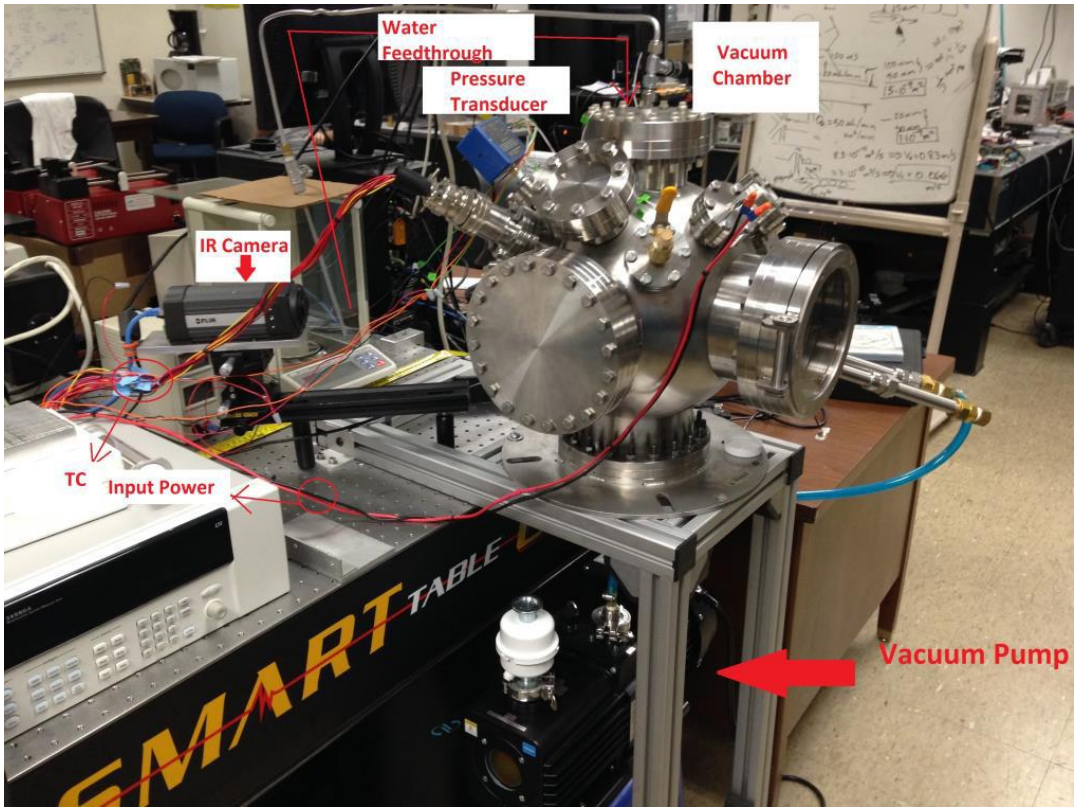

Figure 3.8: The actual test set-up

During initial trials, the vacuum pressure was fluctuating and could not be maintained at 760 Pa. Before testing, the system could reach as low as 200 Pa. During testing, there was 2g/min water vapor being generated inside the vacuum chamber and this amount of vapor had to be removed immediately. The vacuum pump is lubricated by mineral oil and high moisture in the air contaminates the oil so that the vacuuming capability is degraded. Since the vacuum pump was not designed to remove vapor, the amount of water vapor generated from the evaporation process overwhelmed the vacuum performance. 2000 Pa was the average steady-state vacuum level that could be maintained during testing with the evaporator. One solution taken was spreading silicone desiccants inside the vacuum chamber. It did help remove the vapor but not to the extent

that the vacuum level could be lowered to 760 Pa. The ultimate solution was to add a cold trap system along the vacuum line so that water vapor could be condensed in the cold trap before going into the pump. Figure 3.9 is a typical data plot from one test with desiccants inside the chamber.

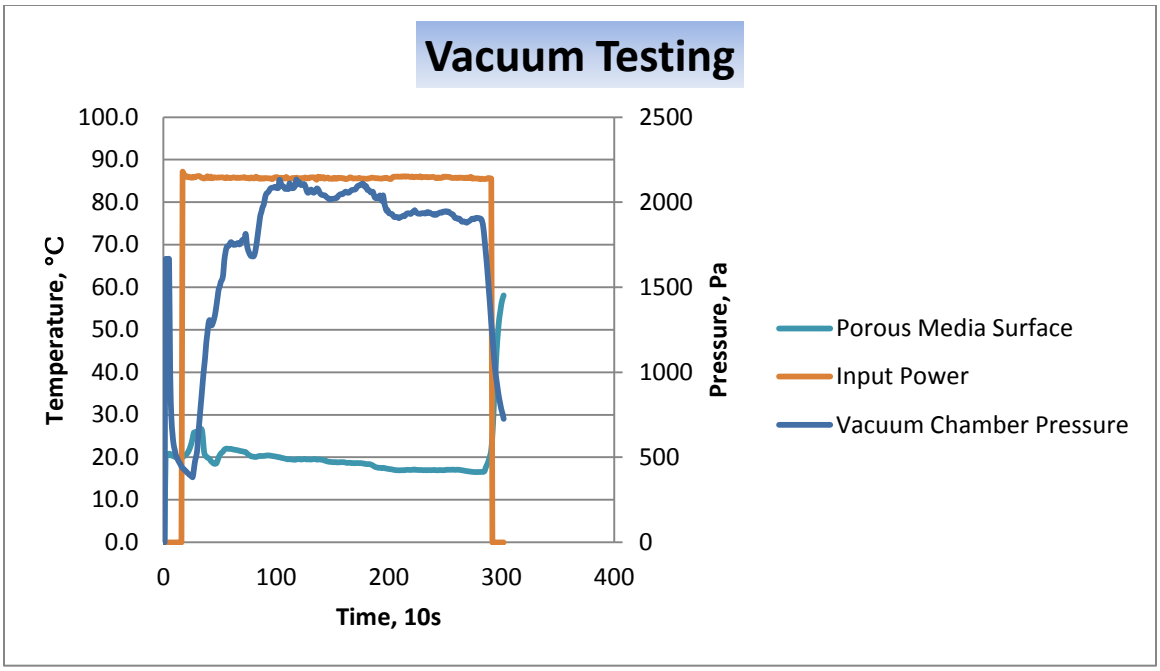

Figure 3.9: Vacuum testing results. The heater and water delivery line was turned on at about the same time. The water flow rate was maintained around 1g/s. The chamber pressure increased due to introduction of vapor. The prototype surface temperature stabilized and had a decreasing trend.

The input power was constant at 87 W. The vacuum pressure fluctuated around 2000 Pa. The average temperature over the PM surface was quite stable around 17°C. The temperature reading was stabilized because the heat provided by the heater and the cooling power rate provided by water evaporation were close to each other.

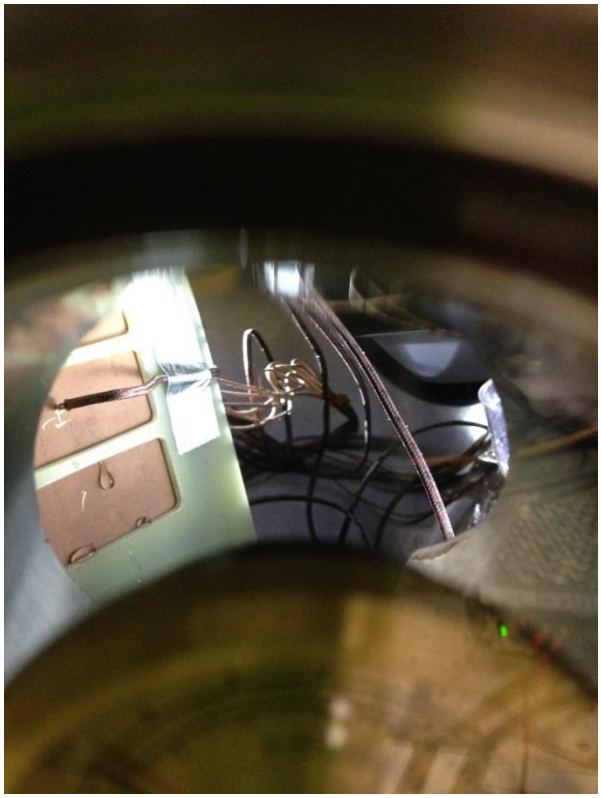

Figure 3.10: Flooding observed on the PM surface during testing

Comparing to the saturation temperature at 2000 Pa, which is 12°C, the PM surface temperature was 5°C higher. The reason could be the pressure drop provided by the PM layer was not high enough. When liquid water travelled through the PM and arrived on the surface, the water pressure was still higher than the ambient pressure and this lead to a higher boiling point and eventually lowered evaporation efficiency. That is a higher steady-state temperature and dripping droplets were observed. These issues could be solved by producing a PM layer that is able to provide a desired pressure drop. A specific study on the PM was carried out to understand its micro-structure.

3.3 HYDROPHOBICITY OF SINTERED COPPER POROUS MEDIA

As discussed before, the role of the copper porous media is to provide enough pressure drops so that the water delivered from the reservoir to the porous-media surface expands to saturation conditions that ensure proper evaporation. If the surface is hydrophobic, the pressure drop through the porous media cannot reach the saturation condition. In order to make the porous media hydrophilic, two subsequent treatments were performed: plasma cleaning and hydrochloric acid treatment. Briefly, the porous media was cleaned by oxygen plasma for 5-6 minutes and subsequently soaked into 0.5M HCl solution for 20-30 minutes. The procedure was determined by the parametric tests done beforehand, as shown in Figure 3.11.

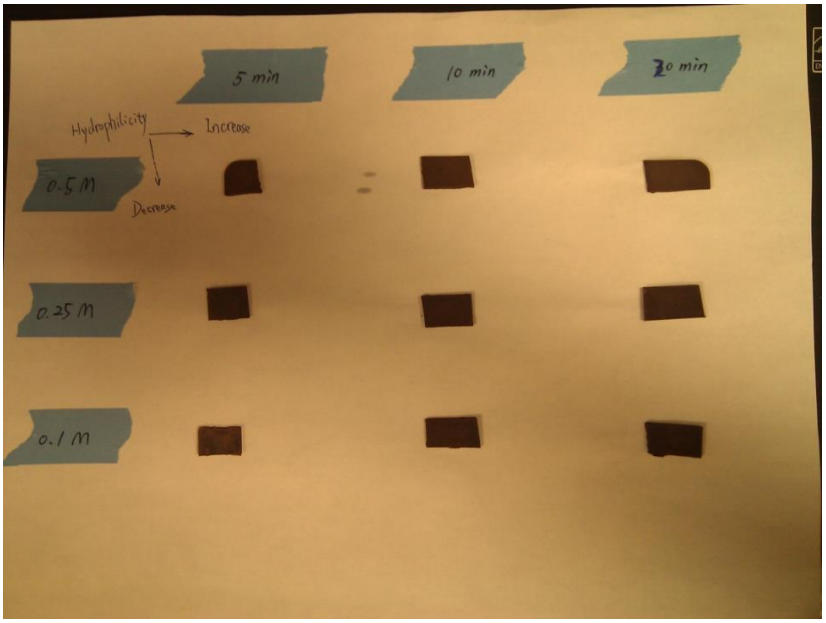

Figure 3.11: Parametric tests on porous media

To characterize the hydrophobicity of sintered copper porous media, these two different parameters: soaking time and molar concentration of HCl solution were involved. As the molar concentration of HCl and treating time period were increased, the

hydrophilicity of the sample tends to increase. Furthermore, after HCl treatment, exposure to the air instead of keeping it in the vacuum was found to help samples stay hydrophilic for a long period. One thing to be noticed is that the color of the sample directly exposed to the air after treatment became darker, which is due to the formation of a thin layer of copper oxide. To investigate changes in structure of the HCl treated sample, SEM was used to image the sample surface structure, as shown in Figure 3.12.

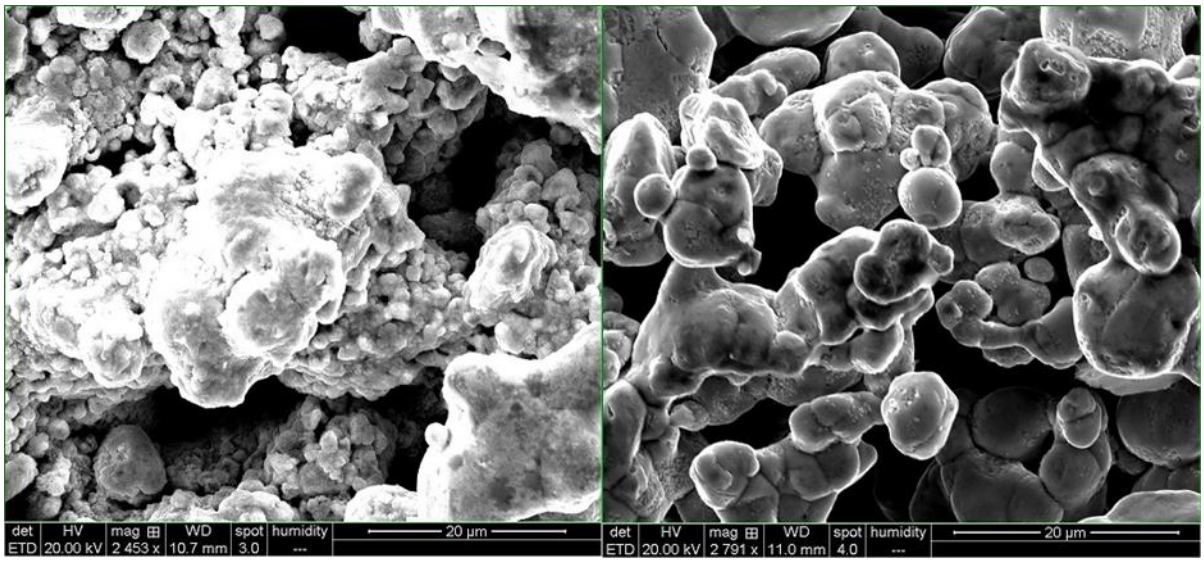

Figure 3.12: Sample one (left) was exposed to the air after treatment while sample two (right) was kept in the vacuum

In the figure above, the rough surface on the sample one is due to the exposure to HCl and presumably this HCl treatment leads to the hydrophilic surface. On the other hand, the smooth surface on sample 2 makes the sample hydrophobic.

The results presented so far were obtained from samples sintered by MIT. For better systematic evaluations of PM samples to be used in the vacuum testing setup, a standard sintering procedure was being developed to meet the growing testing need, which will be addressed in the next section.

Chapter 4: Fabrication and characterization testing

4.1 IEECU COOLANT LOOP FABRICATION--STAMPING

The IEECU coolant loop design shown in Figure 2.1 is formed by two symmetric fin structures. Each fin structure has 15 mini channels engraved on top, which are designed for water delivery. For ease of manufacturing and thanks to iterated surface geometry, each fin structure can be split into 15 identical segments and each segment is equipped with one mini channel in the middle, as shown in Figure 4.1.

Figure 4.1: The original PM design (left) and 1/15 of each IEECU fin surface (right)

The fins are made of copper 101 alloys and the thickness of each fin is 0.5 mm, so stamping tends to be the most cost-effective method for both prototype fabrication and manufacturing. A female and a male mold are required for stamping purpose.

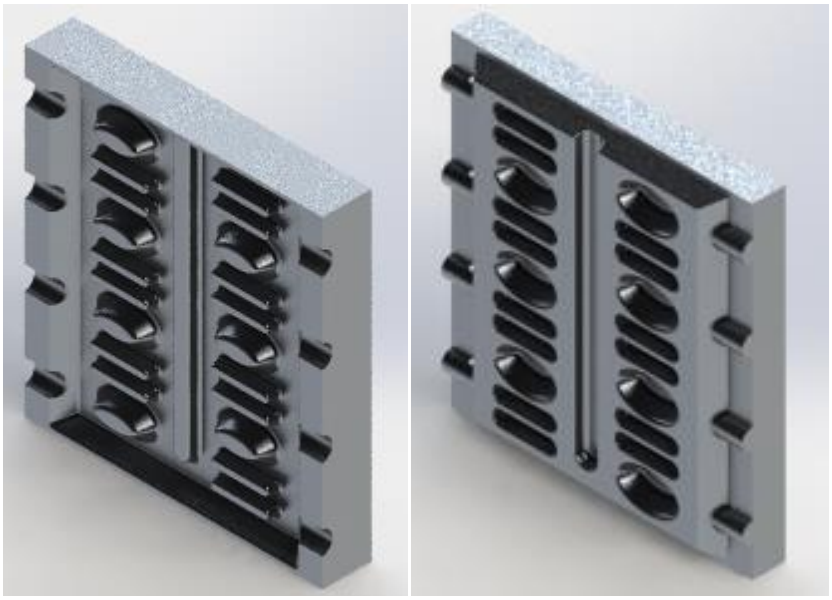

Figure 4.2: The male mold (left) and the female mold (right)

As explained earlier, the figure above only demonstrates one complete segment on the IEECU fin surface and there are 14 other identical segments lined up on the surface. Solidworks files of these molds were created, and with CAE techniques, they were CNC machined by the machine shop at UT Austin out of 7075 aluminum alloy, due to its strength and machinability. Once completed, a metal sheet was stamped by these two molds in a hydraulic press to form fin halves. Aluminum sheet was first tested as a control group. When the hydraulic press force reached 1ton, the aluminum sheet began to shear under stress while the fin features did not come out completely.

Figure 4.3: Failed aluminum sheet under 1 ton

There are many advantages of using copper over aluminum. Copper is more ductile and has better thermal conductivity. For the porous media design, the porous layer was made of copper powder, during sintering process, it was much easier to form bonding between the PM layer and evaporator fin when they were made of the same material. Complete pressing of the evaporator fin with the copper sheet was attainable around 8 ton, but severe shears occurred at multiple locations, especially in the corners of dimples and horizontal slots, as shown in Figure 4.4.

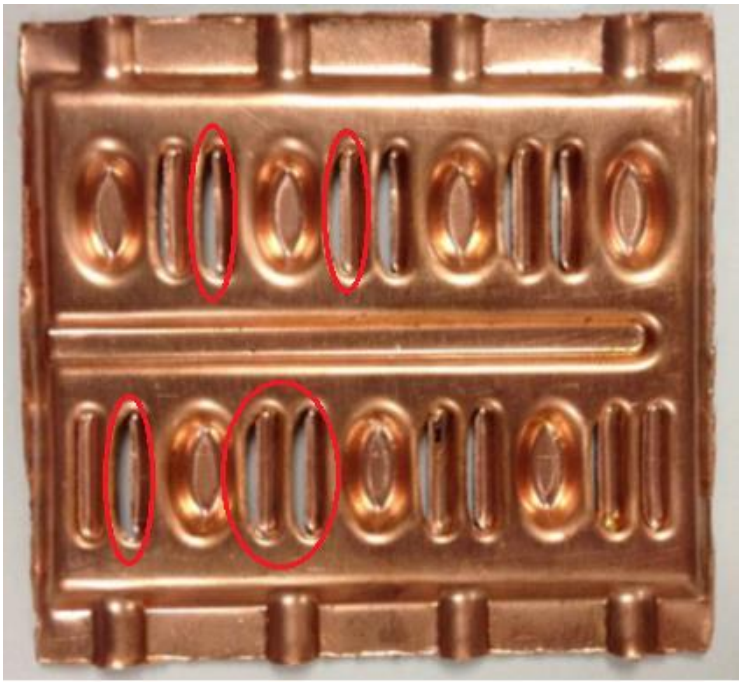

Figure 4.4: Sheared copper fin half by the hydraulic press

Multiple stamping trials have been performed and due to lack of alignment during pressing, some of the surface features on the molds deformed under high pressing force.

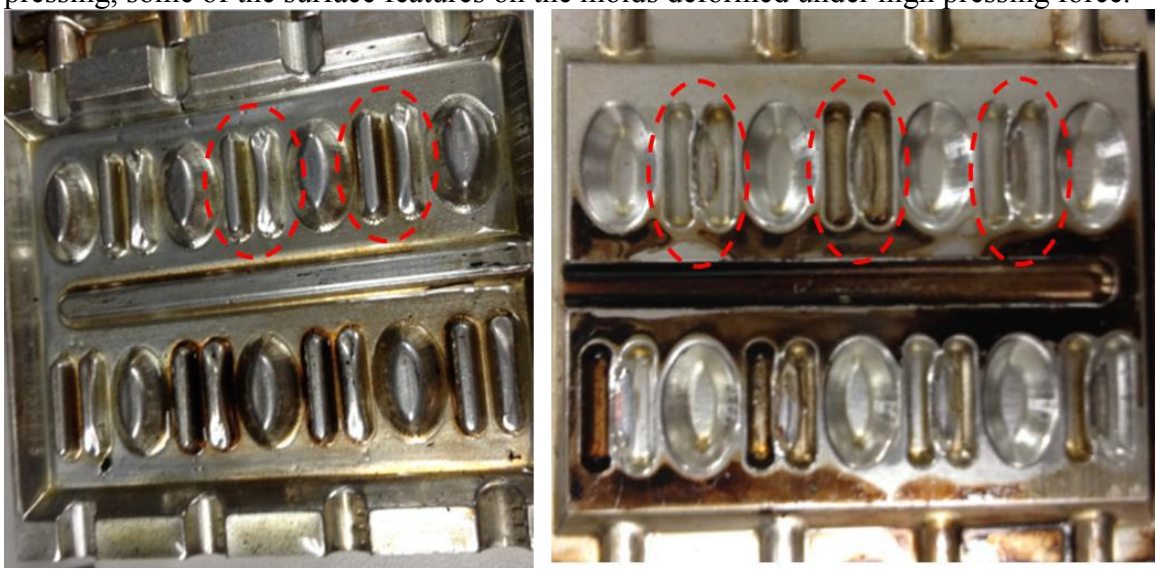

Figure 4.5: Deformed molds due to misalignment

To solve the shearing issues, the heights of the slot features on the male mold were machined down by half. However, this still resulted in shearing in the slots. Consequently, the slots were removed and dimple heights were machined down by half to avoid any possible shearing sources, shown in Figure 4.6.

Figure 4.6: The male mold with slot features removed and dimple features tapered

The female mold, as shown in Figure 4.2, was unchanged since only the male half needed to be modified. Figure 4.7 shows a completed fin half with no slot features and tapered asymmetric dimple features, where no shearing or any other defects could be observed by visual inspection. With two completed fin halves, different bonding methods including brazing, soldering, cold-weld adhesive and silicon adhesive methods were

feasible methods to apply. Soldering was chosen because the process required a relatively lower temperature comparing with brazing while still providing a strong enough mechanical bond, as seen in Figure 4.7.The solder held the fin halves tightly and a water-tight test was carried out to further confirm. Cold-weld adhesive method could hold two fin halves as well, but it took a long time to cure and was difficult to predict the endurance in the liquid-submersion environment. A silicon adhesive method did not cure adequately to hold the fin halves together.

Figure 4.7: Soldered fin halves

3/16'' copper tubes were also soldered on the prototype to facilitate rubber hose attachment, as seen in Figure 4.8.

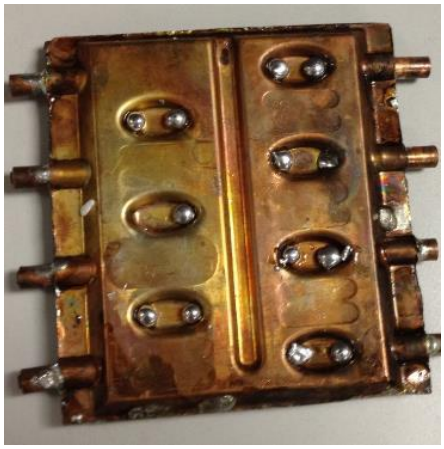

Figure 4.8: Completed IEECU segment prototype

A 5.7 LPM water flow rate into the prototype was set up by a pump, as shown in Figure 4.9. The gaps surrounding the prototype were properly sealed by the soldering process while water leaked from several locations on the surface, especially around the dimple corners, which can be seen in Figure 4.8. Additional solders were applied to fix the leakage. Immersion bath tests were followed up to ensure tight sealing. Finally, a liquid-tight IEECU prototype segment was fabricated and it was also air-tight at relatively low pressures.

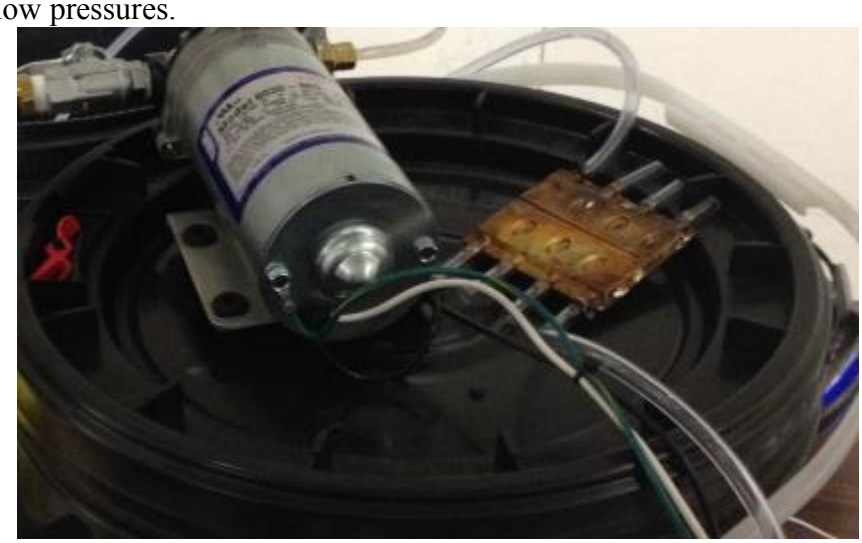

Figure 4.9: Prototype was tested under water pressure and liquid flow inside

Despite a few changes, this prototype was used for characterization tests later on. A redesign of the IEECU fin surface was required to eliminate shearing while not sacrificing too much heat transfer performance. Alignment pins were added in the mold design to avoid misalignments during pressing.

4.2 IEECU COOLANT LOOP FABRICATION—PM SINTERING

In the porous media-based IEECU design, copper porous structures with a target porosity and permeability are required to be properly sintered on the surface of the evaporator as a medium for water transport. The detailed sintering procedure was

provided by MIT. To achieve a 2000 Pa pressure drop across the porous media, 10-50 μm copper powder was sintered under 850-900°C in a vacuum or purged-gas furnace for 45-60mins, as seen in Figure 4.10. A base plate made of graphite was used to support the prototype sample. During trials, copper powders bonded together to form a porous layer and onto copper plates, as seen in Figure 4.11.

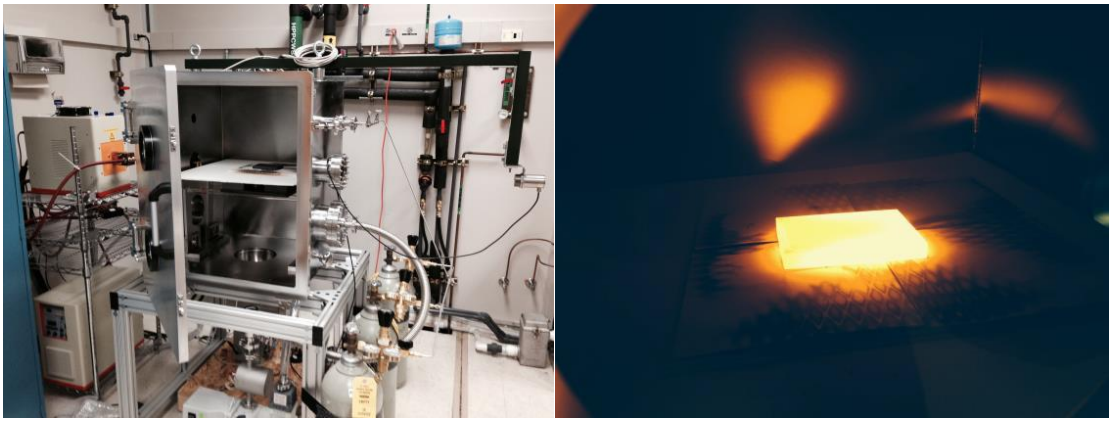

Figure 4.10: The induction furnace for sintering (left) and inside the furnace at 900°C (right)

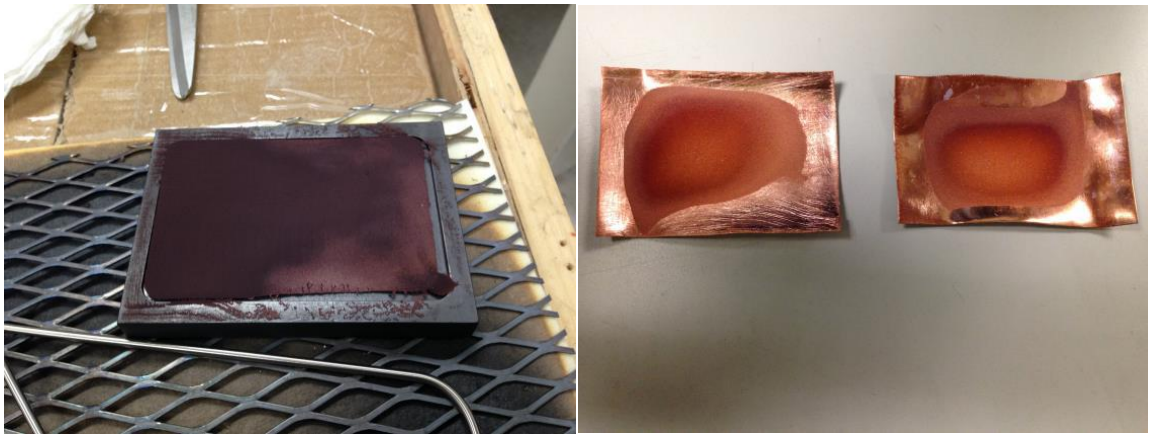

Figure 4.11: A sintered sample on a graphite plate (left) and pure copper plates (right)

During sintering, the mini channel was filled with graphite powders so that the copper porous structure would not block the channel. After this, two fin surfaces with copper porous media were brazed together to form a complete prototype segment.

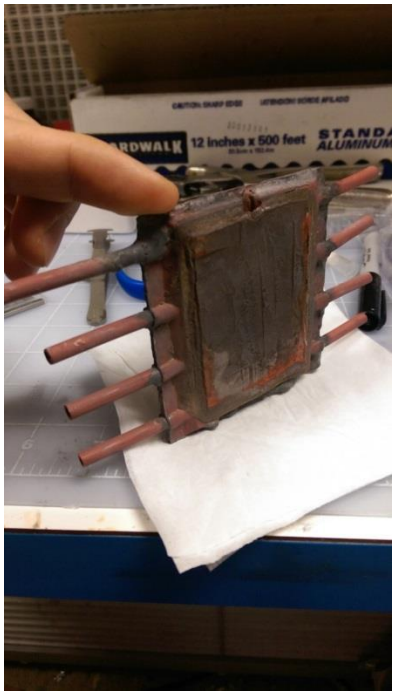

Figure 4.12: A complete prototype segment ready for vacuum testing

4.3 HEAT TRANSFER CHARACTERIZATION TESTING ON IEECU

Characterization experiments were performed to validate theoretical analyses on the original IEECU design and characterize its heat transfer performance under different flow rates.

The 1/15 scaled evaporator segment was fabricated as described earlier. As the first step, ambient tests were favored since the set-up requires less work to build. To mimic the operating conditions in the ATB system, a constant water bath was chosen based on the assumption that IEECU surfaces should be maintained around 3°C during

operation due to evaporation. During experiments, the prototype segment was submerged in a water bath, in which 3°C constant-temperature water was circulating, as shown in Figure 4.13.

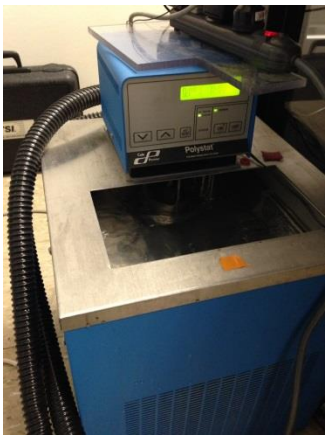

Figure 4.13: The constant-temperature water bath

100% Ethylene Glycol (EG) was used as coolant in the system. It was contained in a reservoir initially. As seen in Figure 4.14, a diaphragm pump sucked EG from the reservoir and pumped it through a flow meter (Omega FPR 300), which was used to monitor the flow rate.

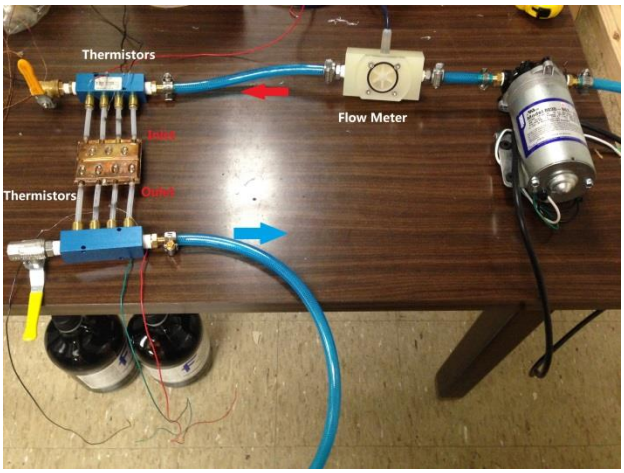

Figure 4.14: The flow loop for IEECU prototype segment testing

Then, the flow was split into four streams by a manifold and went into the prototype segment through the copper tubes attached to it. Four streams of EG flow came out of the prototype segment and were merged by the other manifold into one flow out of the system. The EG coming out was collected by a separate reservoir for subsequent testing reuse. Besides the flow rate, thermistors were positioned at the inlet, outlet and surfaces of the IEECU prototype segment so that temperature measurements at these locations were also recorded.

EG inside the reservoir was heated up to around 45°C. The purpose of pre-heating EG was to increase the temperature differential between EG and the ambient environment, which was set to be 3°C, so that the temperature drop across this segment was significant enough to be detected by the thermistors. Figure 4.15 shows the set-up during testing. Red tape was used to help seal thermistors in position and thermally insulate EG from the water bath environment during the test.

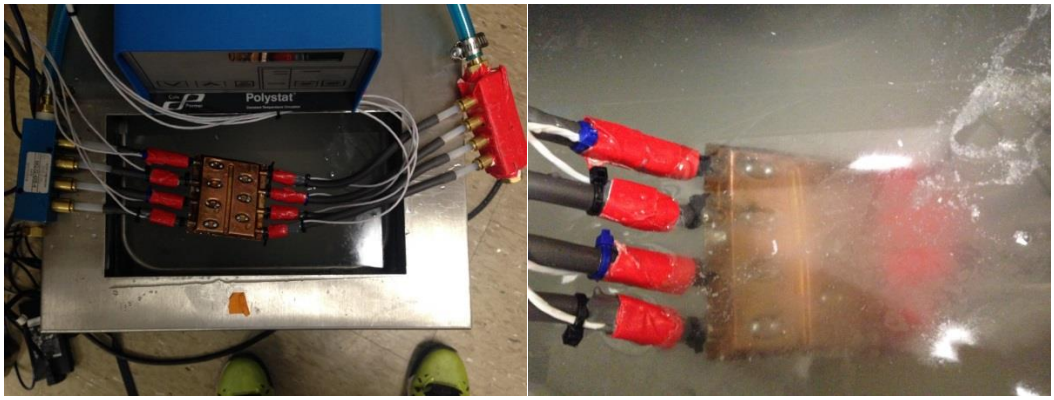

Figure 4.15: Thermistors were insulated right outside inlet and outlet (left); the IEECU prototype segment was submerged in the water bath (right)

Tests were conducted for varying flow rates, as seen in Table 4.1. The flow rate was changed from 1.8L/min to 5L/min, with temperature drops for EG across this 1/15 scale IEECU prototype segment between 2.3 °C and 4.5 °C.

Table 4.1 Experimental results under varying flow rates

Flow Rate, L/min	In_Temp, °C	Temp Drop, °C
1.18	44.9	4.5
1.78	41.8	3.7
2.54	41.6	3.2
3.90	43.2	2.6
4.92	45.7	2.3

Based on Equation 4.1 [16], a correlation between heat transfer coefficient and EG volumetric flow rate was derived, as shown in Figure 4.16.

$$\frac{T_m(x)-T_s}{T_{m,i}-T_s}=\exp(-\frac{P\bar{h}}{\dot{m}C_p}x), \quad \text{for constant surface temperature}$$

Equation 4.1: Internal flow convection in the case of constant surface temperature

To estimate the total temperature drop across the entire IEECU, which is comprised of 15 identical segments, a couple of assumptions have to be made. The first assumption was that the correlation obtained for 1/15 scale IEECU prototype segment also applies to the remaining 14 segments connected in series. The second assumption is that the surface temperature of the IEECU is constant at 3 °C due to evaporation.

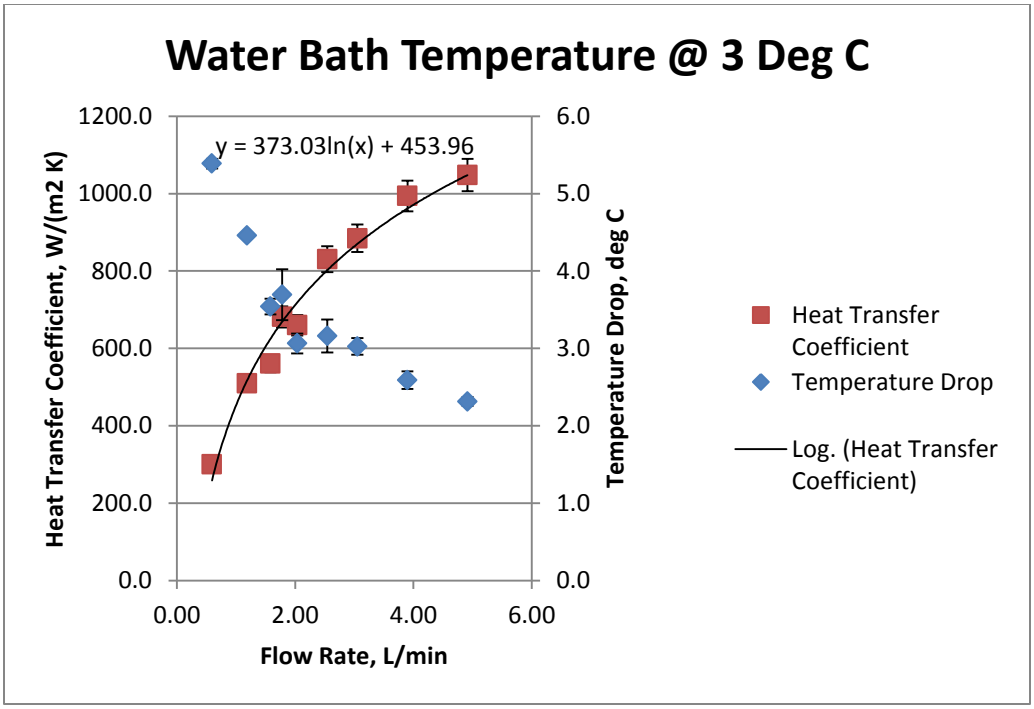

Figure 4.16: Characterization test results under varying flow rates (inlet of EG at 43 °C)

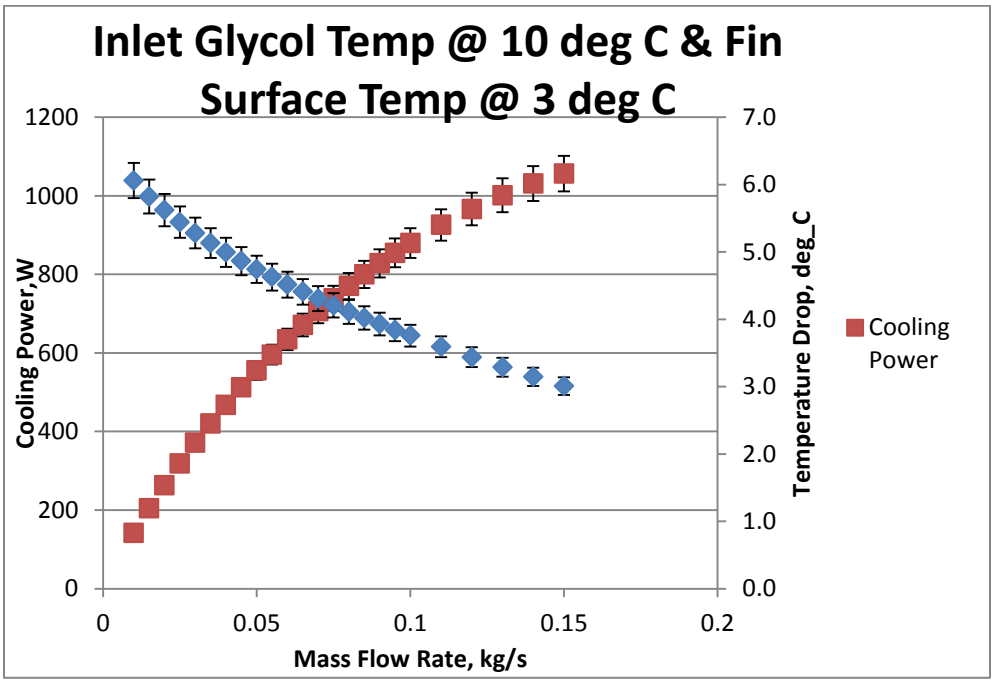

Figure 4.17: Heat transfer estimation on full evaporator fin

Based on analysis in the design phase, 5.67L/min is the desired flow rate of EG to guarantee 2.5 kW cooling power and 7-10 °C temperature drop across the IEECU. However, results in Figure 4.17 showed that at the designated flow rate 5.6L/min, the cooling power is only 1.2 kW, which is about 1.3 kW lower than the target. This lead to reconsideration of the multiple assumptions made at the beginning.

In order to map the real surface temperature distribution of the 1/15 evaporator as well as the average temperature over the entire segment surface during the testing, three thermistors were added on each side of the segment. As shown in Figure 4.18, those thermistors were positioned evenly on the segment surface (two outer surfaces and one dimple surface). Experimental results showed that the average surface temperature across the segment was much higher than the original assumption of 3 °C. For example, at the flow rate of 1.18 L/min, the surface temperature was 14 °C, which indicated that the cooling performance of the design was underestimated. More accurately speaking, the water bath environment is closer to a free convection environment than a constant temperature environment. In order to experimentally find out the average convection coefficient of water inside the bath, a joule heater was installed in the water bath and its steady-state surface temperature was measured given a known power input, as shown in Figure 4.18. When the bath temperature was set to be 3 °C, the convection coefficient of water flow in the bath could be characterized using Equation 4.2, which turned out to be around 900 W/ (m^2K).

$$Q = h*(T_{ext} - T)$$

Equation 4.2: Inward heat flux equation

In addition, the external bath temperature was monitored by three thermistors away from the IEECU segment. The T_{ext} turned out to be 4.7 °C at the steady state.

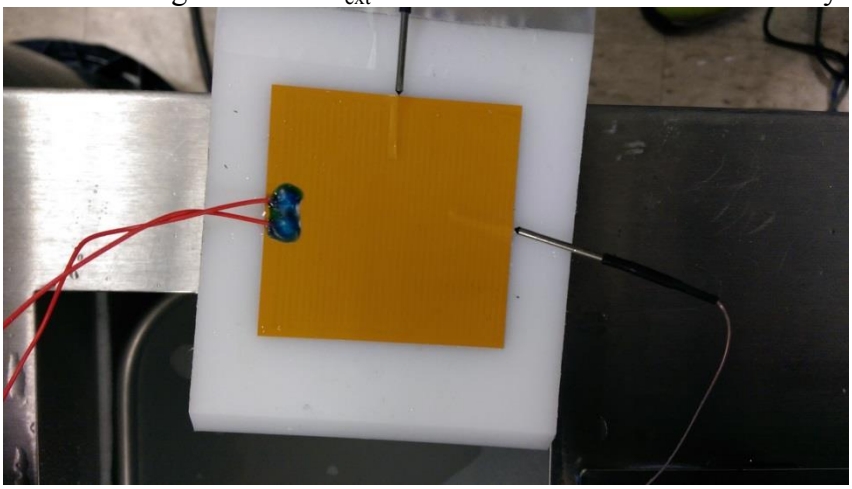

Figure 4.18: A joule heater with thermocouples embedded underneath the surface

COMSOL Multiphysics has been used throughout the testing phase to match simulation with experimental results.

4.4 HEAT TRANSFER SIMULATION ON IEECU

The target heat transfer rate for the IEECU is 2.5 kW and based on pre-design analysis, the original design should be able to provide this magnitude of heat transfer. Unfortunately, the slot structures were taken off due to consistent shearing issues during stamping process. The dimple and slot structures were deemed indispensable to reach the target heat transfer rate and desired temperature drop across IEECU. Before the characterization tests, COMSOL simulations were carried out on the mold design without dimple or slot structures. Because of the symmetric geometry and flow pattern, only one side of the fin surface was modeled and analyzed using COMSOL, as seen in Figure 4.19. From the figure, there are three domains and they are EG domain, copper domain (fin surface) and water vapor domain from left to right. Following the direction of the arrows,

EG enters from one end and leaves from the other end. Since only steady-state scenarios were considered, proper boundary conditions have to be defined in order to obtain accurate results. Critical boundary conditions have been summarized in Table 4.2.

Table 4.2: Important boundary conditions defined

Boundary	Boundary Condition
EG inlet	Constant mass flow rate
EG outlet	Constant pressure
IEECU fin surface	Constant temperature at 3°C
Others	Symmetric

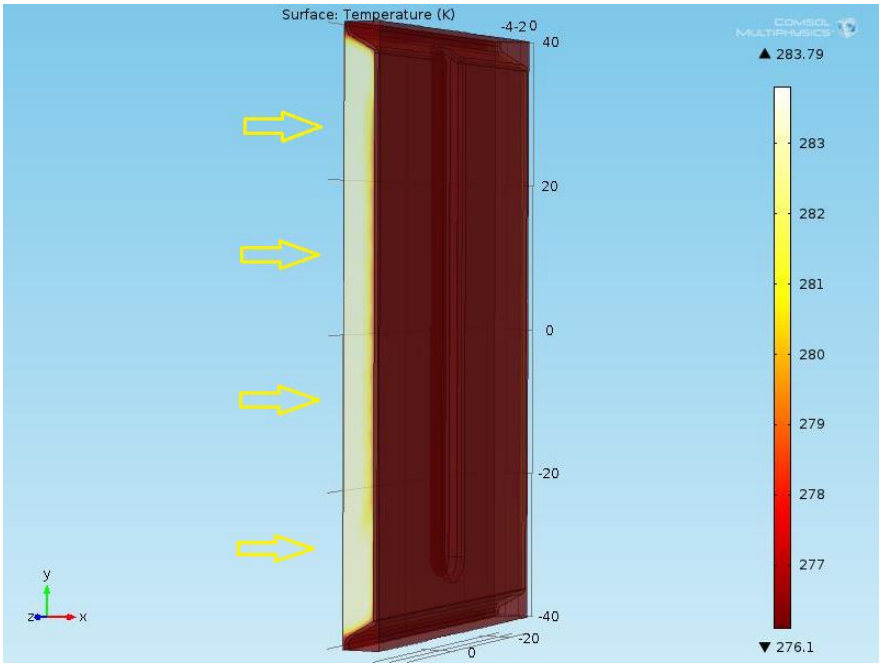

Figure 4.19: Simulation on one half of IEECU prototype segment

The COMSOL simulation predicted that half of the 1/15 scale mold dissipated 840 W. If applying the same result to the full model, which has 15 identical segments of this prototype segment, the total heat dissipation would exceed the target value of 2.5 kW.

However, the discrepancy between estimation from characterization testing results and simulation implies that the boundary conditions need to be redefined. One of the most critical boundary conditions mentioned in Table 4.2 is the IEECU fin surface temperature. Instead of assuming constant surface temperature on the outer fin surface, the boundary condition was changed into "inward heat flux" in COMSOL, which is governed by Equation 4.2, where both h and T_{ext} have been determined by experiments. After rerunning COMSOL under the new boundary conditions, the discrepancy got within the uncertainty range (±0.1°C) of the thermistors used, shown in Table 4.3.

Table 4.3: Simulation in comparison with experimental results

Flow Rate, L/min	In_Temp, °C	Temp Drop, °C	Comsol TD, °C
1.18	44.9	4.5	4.7
1.78	41.8	3.7	3.6
2.54	41.6	3.2	3.0
3.90	43.2	2.6	2.4
4.92	45.7	2.3	2.0

Figure 4.20 demonstrates the flow pattern and EG temperature map inside half of the IEECU prototype segment. The internal flow reaches the highest velocity adjacent to the dimple and mini-channel structures. The local temperatures around these structures are also relatively higher, due to collision of flow.

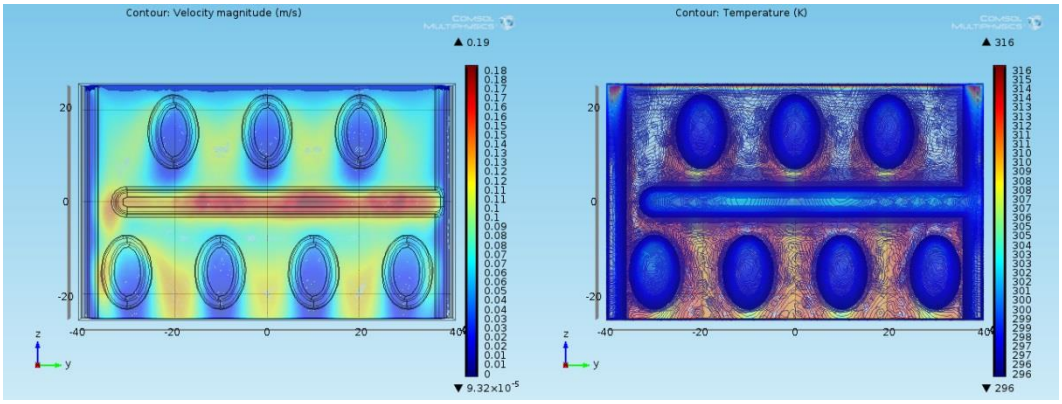

Figure 4.20: Velocity (left) and temperature (right) profile at flow rate 1.18L/min

Based on the results provided by COMSOL, the external thermal resistance was calculated as high as 0.3 (m^2 K)/W, which was about three times higher than the internal resistance at the desired flow rate of 5.6 L/min. The external thermal resistance is the threshold limiting the heat transfer performance here. The thermal resistance of the water bath obtained from the initial experiments was not considered in the initial analyses and it is not the actual mode of operation. But the external thermal resistant appears to be a concern. Future work should be concentrated on finding out what the external heat transfer coefficient is during operation in vacuum.

4.5 REDESIGN THE IEECU

The original design, shown in Figure 4.1, consists of a vertical mini-channel, asymmetric double slot features, and asymmetric dimple features. As explained in the fabrication section, tearing failures kept happening during stamping process on the original design. Although it was expected that the complex surface features would enhance the heat transfer, they are too difficult to manufacture. Consequently, a redesign was necessary and needs to be evaluated at least by COMSOL.

First, the double slot features were removed, as they are spaced too close together. Reducing the height or width did not result in any healthy stamps without shearing. Next, the dimple features were changed in shape from a truncated oval cone to an oval dimple and the height was reduced by 2mm. Furthermore, experiments conducted at MIT showed that a single mini-channel does not provide enough surface area for water vaporization. Therefore, the double slot features were replaced by mini-channel branching-off from the central channel. Compared to the original truncated channel, the new channel design had a smooth round bottom and a reduced height. In summary, both symmetric and asymmetric versions were designed in Solidworks, as seen in Figure 4.21.

Figure 4.21: The redesign of fin half with a symmetric version (left) and an asymmetric version (right)

COMSOL simulations were also carried out on both symmetric and asymmetric designs. Again, only a small segment of the fin surface was modeled due to symmetric geometry in either design. The heat transfer performances were very similar between

these two designs and there is no evidence that one design is significantly better than the other. Since the asymmetric design is equipped with one more branching-off channel, it provides more surface area for water to spread out on the surface, which potentially leads to a better evaporation efficiency and a relatively lower external thermal resistance. Thus, the asymmetric design was chosen to be fabricated and used in the future system integration.

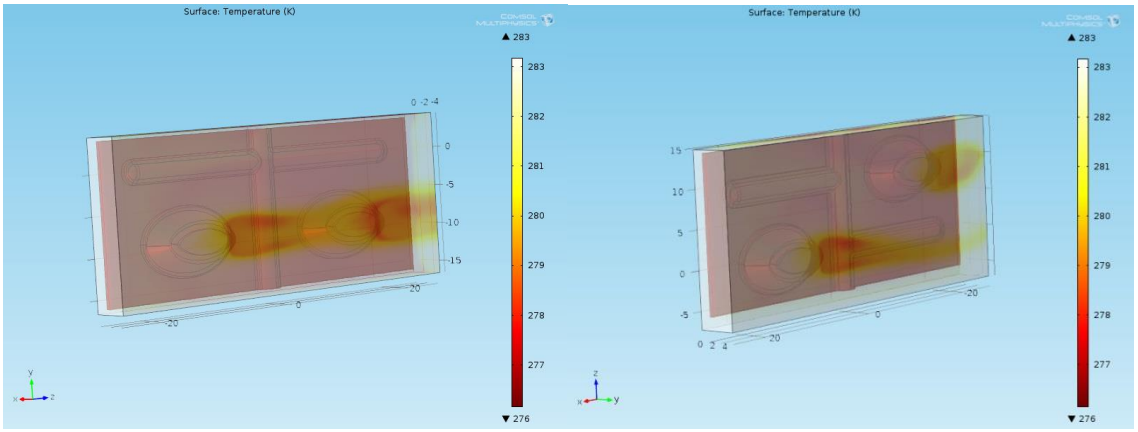

Figure 4.22: COMSOL simulation on the symmetric design (left) and asymmetric design (right)

Chapter 5: ATB System Development

The ATB system, as depicted in Figure 5.1, will be tested using two recirculating loops. One loop is driven by a Lauda-Brinkmann chiller (UC-0080 SP), shown in Figure 5.2 and it is used to cool down the adsorption beds. The other loop is driven by a heater, shown in Figure 5.2 and used for heating up the coolant line. There are external flow meters recording the flow rate of each loop as it is circulated through the bed. The inlet and outlet temperature are also taken using localized arrays of thermocouples at the entrance and exit of the bed.

Regeneration of the adsorption bed will be accomplished by an array of positive-temperature-coefficient (PTC) heaters.

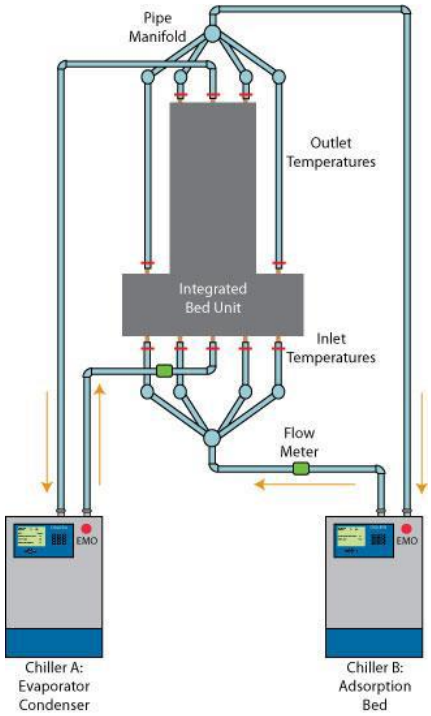

Figure 5.1: The schematic of a system-level testing platform for the ATB

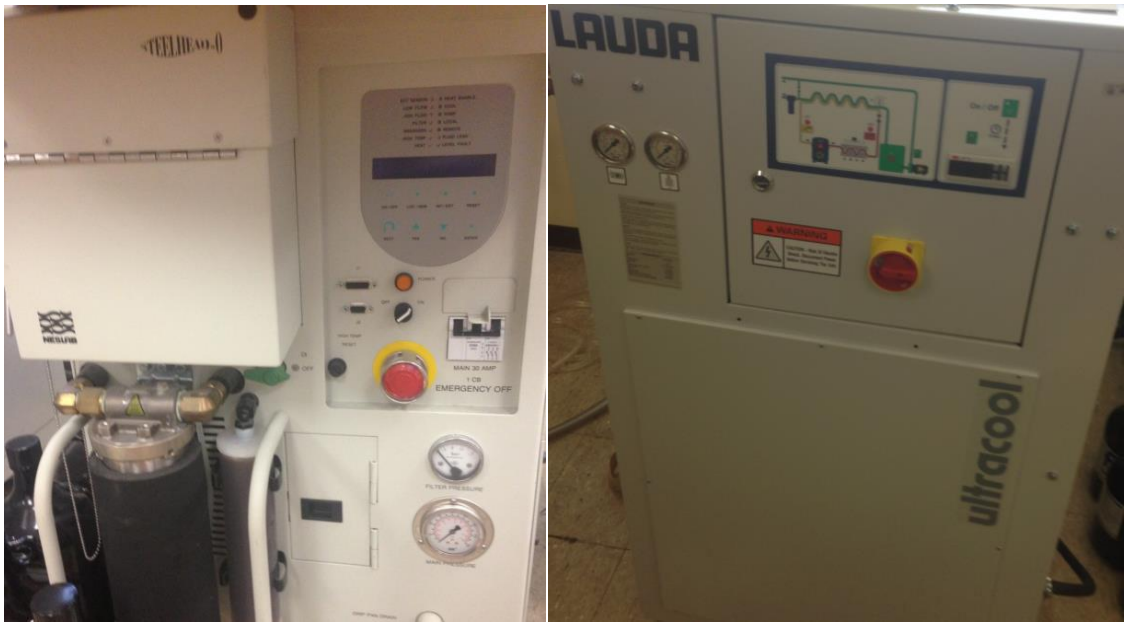

Figure 5.2: The heater unit (left) and cooler unit (right) used in the system testing

In the final system, the monolithic ATB system will require two secondary heat exchangers to interact with the ambient and the cabin air. The vehicle integration work included identifying locations for pumps, tubing and switching valves. As shown in Figure 5.3, in the cooling mode, one glycol pump delivers cold glycol from the IEECU to an air- liquid heat exchanger that would replace the traditional evaporator inside the vehicle HVAC. The second glycol pump would remove adsorption heat from the ATB to be rejected to the environment at the radiator. For the heating mode, the IEECU loop is redirected to be heated at the radiator, and the heat of adsorption is redirected to the air-liquid heat exchanger that now acts as a heater. The use of switching valves reduces the number of tubes used and frees up space for the ATB system.

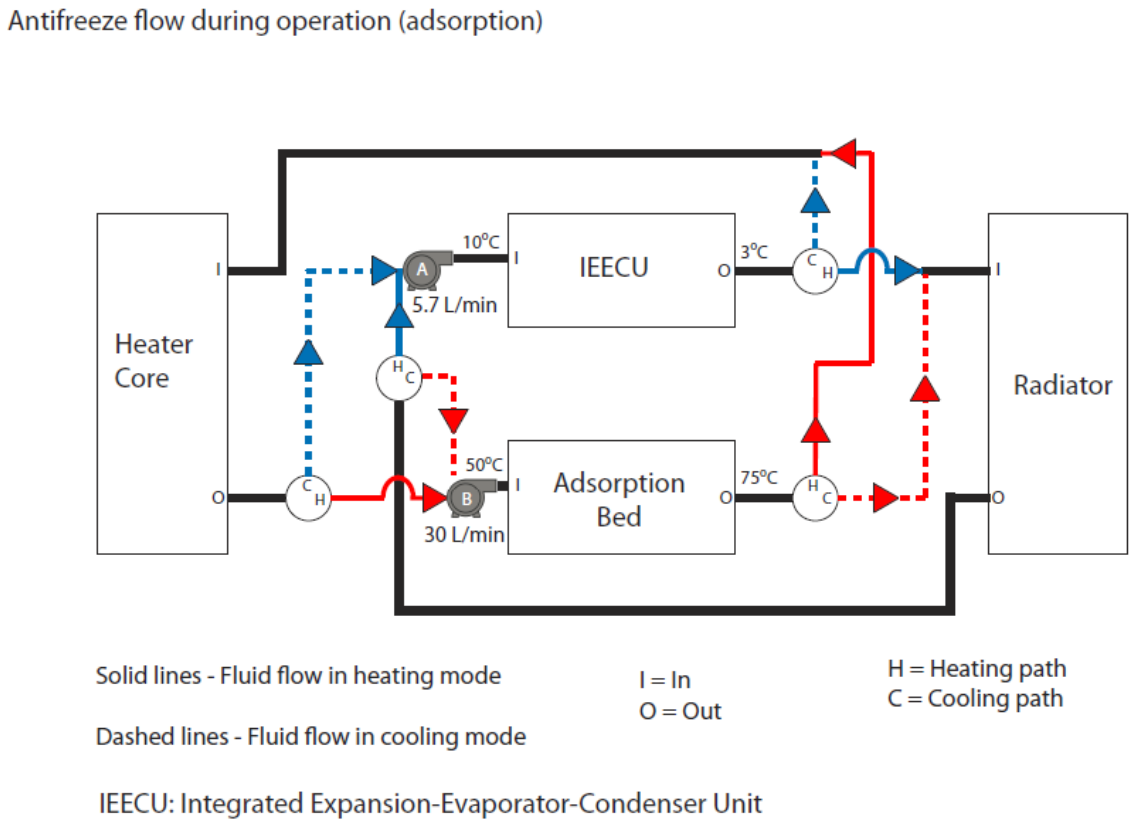

Figure 5.3: Representation of coolant flow loops in the ATB system

The coolant flow conditions and the metric heat transfer rates were used to determine the test conditions for the OEM radiator to be used in the ATB system. The radiator testing setup is shown in Figure 5.4. A small wind tunnel encloses the radiator and allows for unidirectional environmental airflow. The temperatures of inlet and outlet fluids were measured to determine the temperature difference and the heat dissipation by the radiator in conjunction with coolant flow rates.

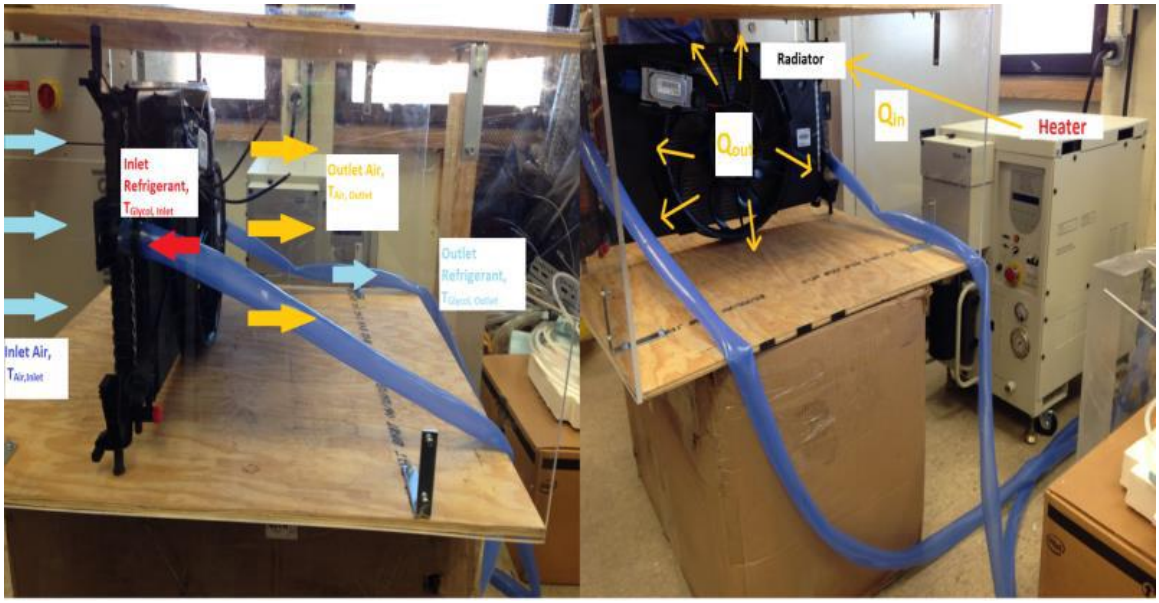

Figure 5.4: Radiator test setup

Two different ambient temperature conditions were chosen to simulate a hot day and an average day. In both scenarios, the required heat dissipation of 4.5 kW was exceeded with the fan running at full speed. On a hot day, 40°C inlet air blows at the radiator and 65 °C EG flows into the radiator at 5.7 L/min, the radiator dissipated 7.5 kW of heat, as seen in Figure 5.5. On an average day, 20 °C inlet air blows into the radiator and 65 °C EG flows into the radiator at 5.7 L/min, the radiator dissipated 8.5 kW of heat. Measured heat dissipation rates suggest that an even smaller radiator can be considered to save on space and weight. The wind tunnel setup used for the radiator testing will also be used for testing the heater core.

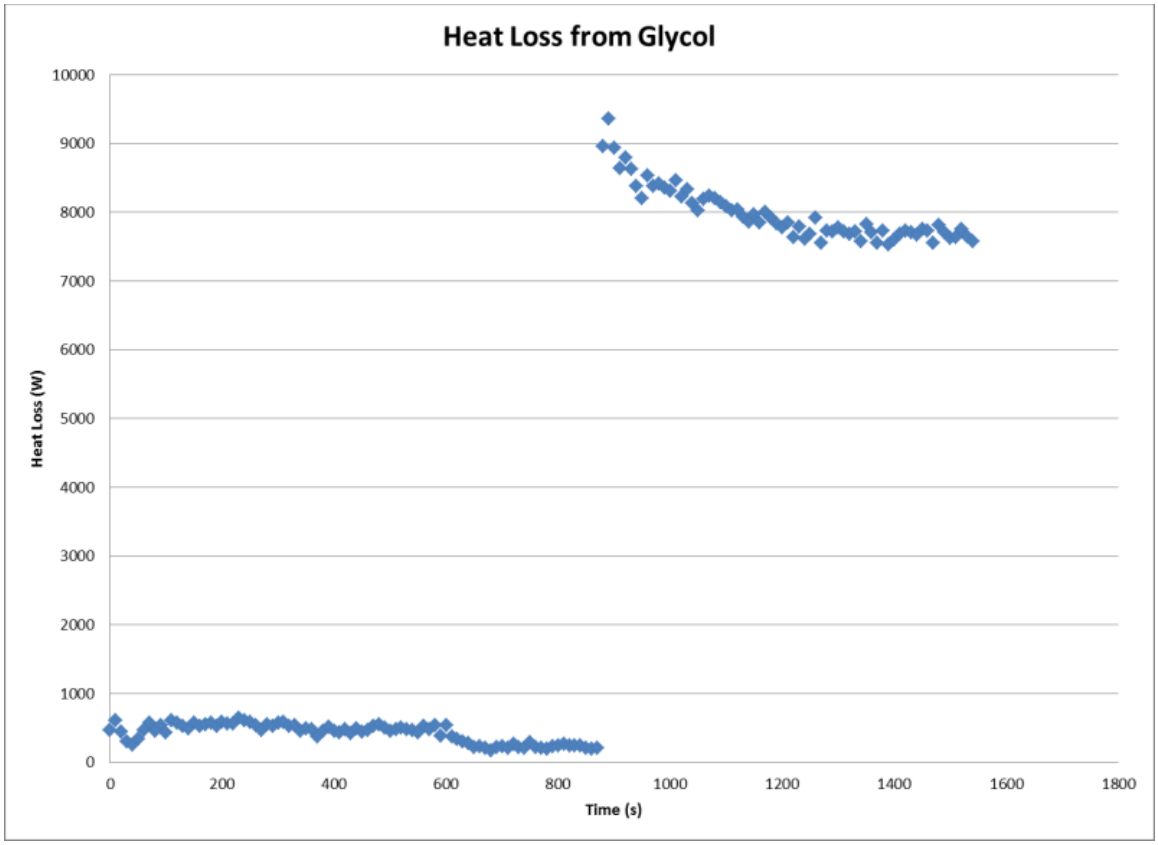

Figure 5.5: Heat dissipated from a radiator on a hot day

The schematics and pictures of the system-level test setup are shown in Figure 5.6 and Figure 5.7. The flow routing schematic includes the glycol heater and chiller, and the optional heat exchanger 1 and 2. They were used to mimic the IEECU and adsorption beds since these components were still under development.

The whole system integration involves assembling of multiple components including radiator and fan assembly, heater core and blower assembly, four switching valves, two glycol pumps, two optional heat exchangers, a glycol heater, a glycol chiller, tubing and adapters, electrical connections, and power sources. Figure 5.7 shows the integrated system components except for the ATB bed.

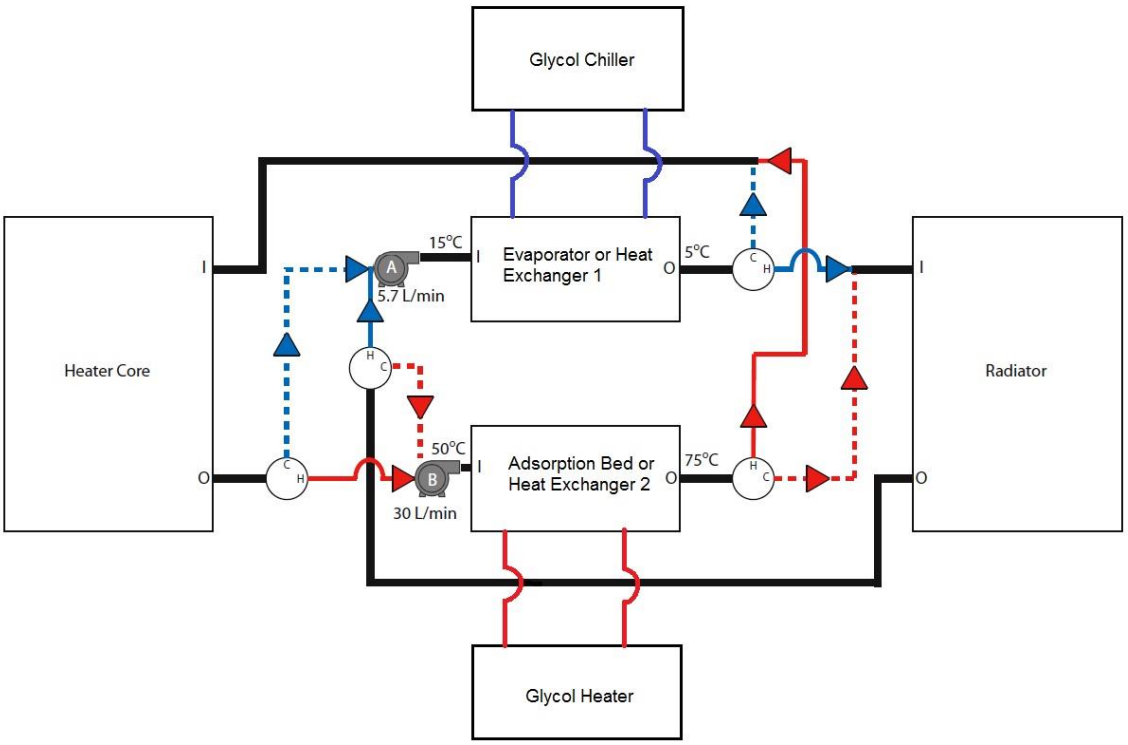

Figure 5.6: Flow routing schematic

Heating and cooling loops connecting essential ATB components were completed and the loops were filled with EG. During preliminary tests, hermetic sealing was pursued and accomplished. In order to check whether EG pumps and switching valves function well, food coloring was injected into individual EG loops for visualization during testing, since EG is nearly transparent like water. Switching valves properly separated between flow loops and re-route the flow when switched, as shown in Figure 5.8. Glycol pumps also worked properly once fully primed with EG. However, pulse-width modulation (PWM) signal needs to be used to adjust pump speed to metric values in the future work.

Figure 5.7: System components involved (top) and a complete system setup (bottom)

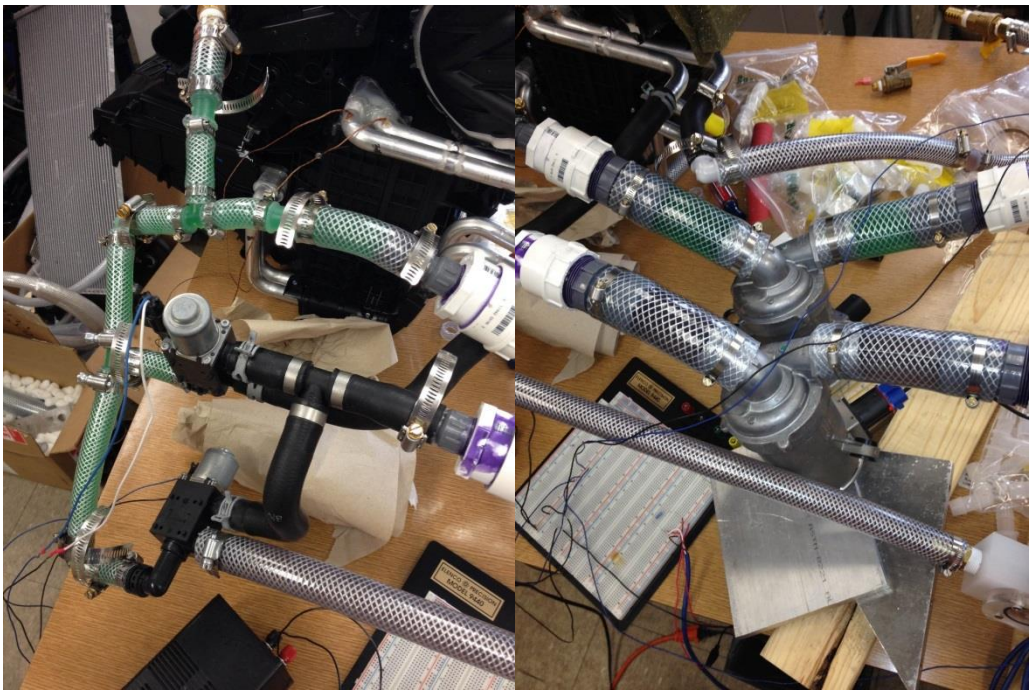

Figure 5.8: Food coloring in the system (left) and glycol pumps (right)

Chapter 6: Conclusion and Future Work

The research summarized in this thesis revolves around the development of an advanced thermo-adsorptive battery climate control system (ATB). The specific focus here is on the development of the IEECU and ATB system integration.

There were two approaches involved in the initial designing phase of the IEECU water delivery system. Both porous media (PM) design and spray cooling design were analyzed from hydrodynamic and heat transfer perspectives. Other factors including pumping power consumption, stability, versatility and manufacturability have also been taken into consideration. Proof-of-concept tests at ambient condition have proven that both approaches have the potential to meet the target metric heat transfer rate of 2.5 kW.

Proof-of-concept testing under vacuum is an important step to understand the working mechanism of ATB operation. It provides relevant knowledge for further prototype testing, and is a platform on which future system integration testing setup is going to be built. In the meantime, it raised several red lights, such as the flooding issue on the PM surface and how to maintain a stable vacuum level for the system.

Fabrication of IEECU fin surfaces introduced several manufacturing methods including stamping, sintering, brazing and micro-drilling. Each process involved many testing runs. Both COMSOL simulations and characterization tests have validated the design and future work need to be concentrated on maximizing evaporation efficiency on IEECU fin surfaces.

A monolithic system has been chosen to enhance the mass and heat transfer inside the system to minimize energy loss. A preliminary system setup has been completed except for a few minor modifications such as the integration of the finalized IEECU prototype and adsorption beds. In the final system testing phase, when a system-level

vacuum chamber is ready, the IEECU and adsorption beds will be installed inside the chamber. This vacuum chamber will replace optional heat exchangers used at present and be connected with other existing components. Instruments including thermocouples and flow meters will be added in and calibration of the whole system will be necessary.

Overall, a PM design-based IEECU was accomplished and validated by COMSOL simulations and the ambient characteristic experiments to meet the 2.5 kW heat transfer requirements. A monolithic system test setup was finished and ready for further calibrations.

References

[1] Jeff Cobb (2014-01-16). "Top 6 Plug-In Vehicle Adopting Countries". HybridCars.com. Retrieved 2014-01-18. Over 172,000 highway-capable passenger vehicles have been sold in the U.S. between 2008 and December 2013.

[2] International Energy Agency, Clean Energy Ministerial, and Electric Vehicles Initiative "Global EV Outlook 2013 - Understanding the Electric Vehicle Landscape to 2020" http://www.iea.org/publications/globalevoutlook_2013.pdf April 2013.

[3] US Department of Energy, http://energy.gov/public-services/vehicles and http://www.fueleconomy.gov/feg/evtech.shtml#end-notes

[4] K. Bennion and M. Thornton, Integrated Vehicle Thermal Management for Advanced Vehicle Propulsion Technologies, SAE 2010 World Congress.

[5] Sand, J. R.; Fischer, S. K., Total Environmental Warming Impact (TEWI) Calculations for Alternative Automotive Air-Conditioning Systems, Presented at 1997 SAE International Congress, Detroit, Michigan, 1999.

[5] No author, Heater Core Database, http://coolercores.awardspace.com/index.html

[6] R. Farrington, J. Rugh, Impact of Vehicle Air Conditioning on Fuel Economy, Tailpipe Emissions, and Electric Vehicle Range, Presented at the Earth Technologies Forum, Washington, D.C., 2000

[7] R. Farrington, J. Rugh, *Impact of Vehicle Air-Conditioning on Fuel Economy, Tailpipe Emissions, and Electric Vehicle Range* (NREL/CP-540-28960, 2000; www.nrel.gov/docs/fy00osti/28960.pdf).

[8] K. Kunze, S. Wolff, I. Lade, J. Tonhauser, *A SystematicAnalysis of CO*2*-Reduction by an Optimized Heat Supply During Vehicle Warm-Up* (SAE paper 2006-01-1450, 2006; http://papers.sae.org/2006-01-1450).

[9] J. Taneja *et al*., *Toward Cooperative Grids: Sensor/Actuator Networks for Renewables Integration* (Proceedings of IEEE SmartGridComm, 2010; http://ieeexplore.ieee.org/xpl/freeabs_all.jsp?arnumber=5621992).

[10] R. Laughlin, *Powering the Future* (Basic Books, New York, 2011), pp. 94–98.

[11] A. Marcos, L. Chow, J. Du, S. Lei, D. Rini and J. Lindauer, "Spray cooling at low system pressure," Semiconductor Thermal Measurement and Management, no. Eighteenth Annual IEEE Symposium, pp. 169-175, 2002.

[12] K. Estes and I. Mudawar, "Correlation of Sauter mean diameter and critical heat flux for spray cooling of small surfaces," International Journal of Heat and Mass Transfer, vol. 38, no. 16, pp. 2985-2996, 1995.

[13] J. L. Yanosy, "Water Spray Cooling in a Vacuum (Dissertation)," University of Connecticut, 1985.

[14] Li, C., Peterson, G., & Wang, Y. (2006, December). Evaporation/Boiling in Thin Capillary Wicks (1) - Wick Thickness Effects. Journal of Heat Transfer, 128(1312).

[15] Dominguez Espinosa, F., Peters, T., & Brisson, J. (2012). Effect of fabrication parameters on the thermophysical properties of sintered wicks for heat pipe applications. International Journal of Heat and Mass Transfer, 55, 7471-7486.

[16] Incropera, F. P., Dewitt, D. P., Bergman, T. L., & Lavin, A. (2007). Fundamentals of Heat and Mass Transfer. Wiley.